Review article

Ji-Hun Kang*, Dai-Sik Kim* and Minah Seo*

Terahertz wave interaction with metallic nanostructures

Abstract: Understanding light interaction with metallic structures provides opportunities of manipulation of light, and is at the core of various research areas including terahertz (THz) optics from which diverse applications are now emerging. For instance, THz waves take full advantage of the interaction to have strong field enhancement that compensates their relatively low photon energy. As the THz field enhancement have boosted THz nonlinear studies and relevant applications, further understanding of light interaction with metallic structures is essential for advanced manipulation of light that will bring about subsequent development of THz optics. In this review, we discuss THz wave interaction with deep sub-wavelength nano structures. With focusing on the THz field enhancement by nano structures, we review fundamentals of giant field enhancement that emerges from non-resonant and resonant interactions of THz waves with nano structures in both sub- and super- skin-depth thicknesses. From that, we introduce surprisingly simple description of the field enhancement valid over many orders of magnitudes of conductivity of metal as well as many orders of magnitudes of the metal thickness. We also discuss THz interaction with structures in angstrom scale, by reviewing plasmonic quantum effect and electron tunneling with consequent nonlinear behaviors. Finally, as applications of THz interaction with nano structures, we introduce new types of THz molecule sensors, exhibiting ultrasensitive and highly selective functionalities.

Keywords: terahertz spectroscopy; optical properties; nanostructures; metamaterials.

*Corresponding authors: Ji-Hun Kang, Department of Physics and Astronomy, Seoul National University, Seoul 151-747, Korea, e-mail: jihun.kang@snu.ac.kr; **Dai-Sik Kim,** Department of Physics and Astronomy, Seoul National University, Seoul 151-747, Korea; and Center for Atom Scale Electromagnetism, Seoul National University, Seoul 151-747, Korea, e-mail: dsk@phya.snu.ac.kr. http://orcid.org/0000-0002-8950-1199; and **Minah Seo,** Sensor System Research Center, Korea Institute of Science and Technology, Seoul 136-791, Korea, e-mail: mseo@kist.re.kr

1 Introduction

The recent development in terahertz (THz) technology enables a wide range of applications in electronics [1–6] and photonics [7–9]; for medical [10–12], military [13–15], and security purposes [16–18]; in microdisplay [19]; and even in the investigation and conservation of cultural heritages [20–22], which is based on its excellent sensitivity and selectivity. Such advances in THz applications have been stimulated by the improvement in functional THz devices such as filters [23–28], switches [29–34], and sensors [35–40]. Artificially structured metamaterials in subwavelength scale, especially, provide us with the ability to control THz responses over the broad bandwidths [41–46], determined by key parameters: length scale [47, 48], geometry [49], and surrounding materials [50, 51]. The dielectric properties of these metamaterials, changeable by optical [24, 52–54], electrical [55, 56], thermal [57–59], or other mechanical [60–62] means, with or without lateral patterns, are in turn used to control transmission or reflection behavior over entire THz frequencies, further extending device performance. THz wave interaction with deep subwavelength nanostructures with extremely high cross-sections will be discussed in this review as introduced with several milestones regarding the structures from micrometer [39, 42, 63–67] to nanometer [68–78] scale and, finally, the Angstrom scales [79, 80] (Figure 1). In particular, the enhanced THz nonlinear phenomena in Angstrom-sized infinite gaps will find unprecedented resonant and nonresonant applications in metamaterials [81–86]. Finally, several novel types of THz sensing technology based on the field enhancement properties using subwavelength structures for variety of chemistry, biology, and medical applications will be introduced.

2 Fundamentals of giant terahertz field enhancement at an infinitely long nanogap

Using the vector Babinet principle, concentrating terahertz (THz) electric field in a small aperture in metal [69,
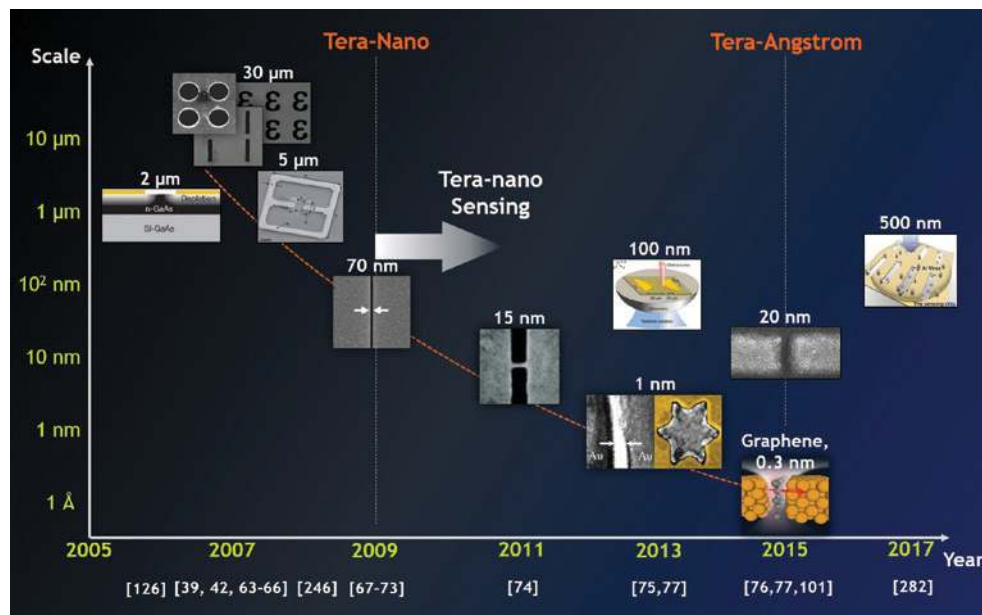
Figure 1: Achieved milestones in THz wave interaction with metallic structures down to the Angstrom scale.

87–92] is equivalent to enhancing the magnetic field of light around rod and patch antennas [93–100]. Although a metal film in THz frequency is neither perfect conductor nor infinitely flat, various areas of THz research [2, 99, 101–115], including THz plasmonics [116–123] and metamaterials [124–130], implicitly use this principle, which remains true in its spirit if not in its rigor. One of the earliest theoretical accounts on the light-aperture interaction had been made by Sommerfeld's half-plane problem [131–133] that was revisited by Bethe and Bouwkamp to deal with small apertures in infinitely thin perfect conducting plates [134–137]. These earlier studies instigated further investigations on the light interaction with periodic aperture systems [138], which were later extended to studies on enhanced light transmission through the apertures in visible [139–141], infrared (IR) [142], and THz [67, 143–146] regimes. To resolve the enhanced transmission and consequent strong field enhancement near the apertures, numerous theoretical schemes such as coupled-mode theory [90, 147–154], microscopic models [89, 155, 156], transfer matrix method [157, 158], and capacitor model [88], incorporated with various numerical methods [40, 159–161], were developed.

Basically, the field enhancement can be explained in terms of macroscopic accumulation of surface charges near the apertures' edges, driven by incident light. The accumulated charges give rise to capacitive enhancement of electric field in the gap [69, 88]. This simple picture paved a way to the gigantic field enhancement supported by deep subwavelength apertures in metal (Figure 2), which is, in particular, essential for THz nonlinear optics [163–169] that requires intense electromagnetic field.

In this section, we discuss THz field enhancement in deep subwavelength apertures. Specifically, we focus on nonresonant THz field enhancement by an infinitely long gap with sub-skin-depth thickness and provide a simple model to explain that the field enhancement can be simply given by a ratio of photon wavelength and thickness. We also discuss a Kirchhoff integral formalism that allows quantitative estimation of field enhancement in the near-field from the far-field measurement. After that, we discuss resonant field enhancement supported by a rectangle slot, exhibiting different behavior of field enhancement compared to the non-resonant case.

2.1 THz field enhancement and skin-depth physics

We first concentrate on metal films of thickness 100 nm or less, satisfying the sub-skin-depth condition at THz regime [67]. Consider, for a good conductor, that the ultimate field enhancement (*FE*) in a high-aspect ratio nanogap of air sandwiched between two sub-skin-depth metallic planes, irradiated by an electromagnetic wave with an incident electric field of E_{inc}, has a simple analytical expression when the gap width w is much smaller than the film thickness h:

$$FE = \left| \frac{E_{gap}}{E_{inc}} \right| = \frac{\lambda}{\pi h}; \; w \ll h, \qquad (1)$$

where E_{gap} is the electric field at the gap, λ is the vacuum wavelength, and h the film thickness [76, 88, 170]. When
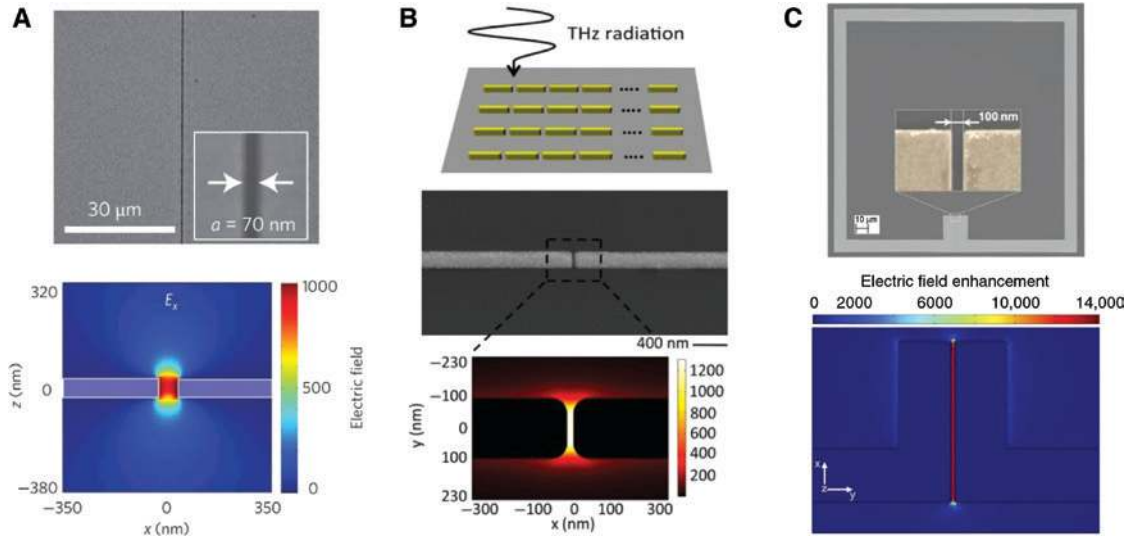
Figure 2: THz field enhancements in various gap structures.
(A) Nanogap in metal plate, (B) nanogap in rod antennas, and (C) split-ring resonators. A, B, and C are reproduced from Refs. [69], [101], and [162], respectively.

the gap is filled with a dielectric of permittivity, ε_{gap}, the formula is modified to, somewhat trivially,

$$FE = \left| \frac{E_{gap}}{E_{inc}} \right| = \frac{\lambda}{\pi h} \frac{\varepsilon_0}{\varepsilon_{gap}}, \qquad (2)$$

where ε_0 is the vacuum permittivity [76]. What is surprising is that the gap *FE* is seemingly independent of how good the metal is.

To derive Eq. (1), we first consider direct transmission of electromagnetic wave through a thin film of free-standing metal; for the sake of simplicity, we assume a normal incidence. For this instance, by a thin film. We mean films whose thickness h is smaller than the skin depth $\delta = \sqrt{\frac{2}{\mu_0 \sigma_m \omega}}$ but larger than a characteristic thickness of

$$h_0 \equiv \frac{2\varepsilon_0 c}{\sigma_m}; \ h_0 \ll h \le \delta, \qquad (3)$$

where σ_m is the conductivity of metal, μ_0 is the vacuum magnetic permeability, and $\omega = 2\pi f$ is the angular frequency of the electromagnetic wave. The characteristic thickness, h_0, at which absorption loss by the metal is 50% is only 0.53 nm for a reasonably good metal of a conductivity 10^7 Siemens per meter ($\Omega^{-1}m^{-1}$), so that any transition metal films of today's technology fall above this thickness. Skin depth at 1 THz is typically 100 nm or more even for good metals so that transition metal films in the range of 5–100 nm thickness satisfy Eq. (3) (Figure 3). For these thin metal films, the amplitude transmission and reflection coefficients, t and r, respectively, are given as

$$t = \left| \frac{E_t}{E_{inc}} \right| \approx \frac{2\varepsilon_0 c}{\sigma_m h} = \frac{h_0}{h} \ll 1; \ r \approx 1 - \frac{h_0}{h} \approx 1, \qquad (4)$$

where E_{inc} is the incident electric field and E_t is the transmitted electric field as described in Figure 4.

To derive Eq. (4), we consider transverse magnetic polarized incident light (E_x, H_y) and focus on the magnetic field of light near the thin film. At the incident surface, reflection makes the magnetic field of light approximately twice that of the incident field, whereas on the transmission side, the magnetic field is much smaller than
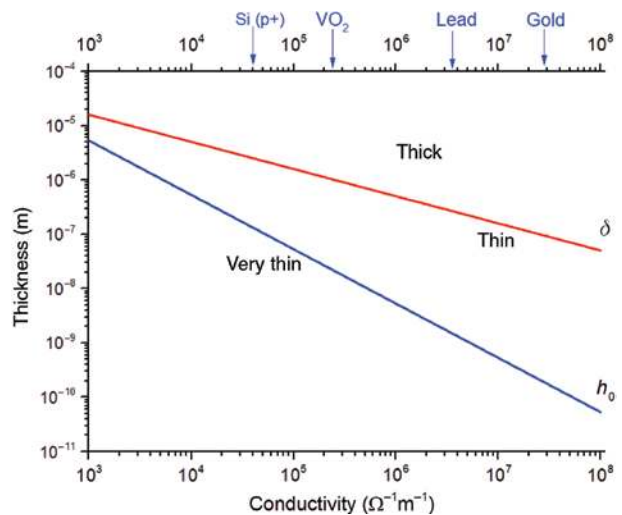
**Figure 3:** Thickness of metallic thin films in terms of conductivity is plotted.
In particular, Si (p+), VO$_2$, lead, and gold cases are denoted in blue arrows. Given conductivities of materials are at 1 THz [171–176].
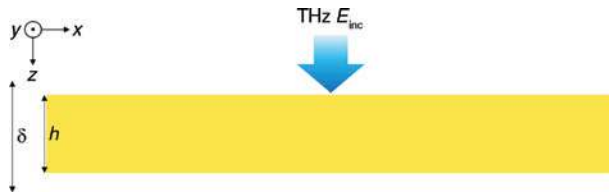
Figure 4: Metallic thin film with a thickness less than the THz skin depth is irradiated by THz field.

the incident field. We assume a constant electric field/current density inside and apply Ampere's law, $\nabla \times H = J$, which gives rise to the current density $J \approx \frac{2H_{inc}}{h}$, ignoring the vacuum displacement-current term. Then, the continuity of tangential component of electric fields at the air-metal interface leads to $E_t = E_m = \frac{J}{\sigma_m} = \frac{2H_{inc}}{\sigma_m h} = \frac{2\varepsilon_0 c}{\sigma_m h} E_{inc}$, resulting in Eq. (4) (Figure 5A). Here, E_m is electric field just inside the metal surface of the transmitting side. Since the normal component of the displacement current is the same across the air-metal boundary of the gap, we obtain $E_{gap} = \left| \frac{\varepsilon_m}{\varepsilon_0} \right| E_m \approx \frac{\sigma_m}{\varepsilon_0 \omega} \frac{2\varepsilon_0 c}{\sigma_m h} E_{inc} = \frac{\lambda}{\pi h} E_{inc}$ having taken advantage of the metal dielectric constant in the terahertz regime

$$\varepsilon_m = \varepsilon_\infty + i \frac{\sigma_m}{\omega \left(1 - i \frac{\omega}{\gamma} \right)} \approx i \frac{\sigma_m}{\omega}, \qquad (5)$$
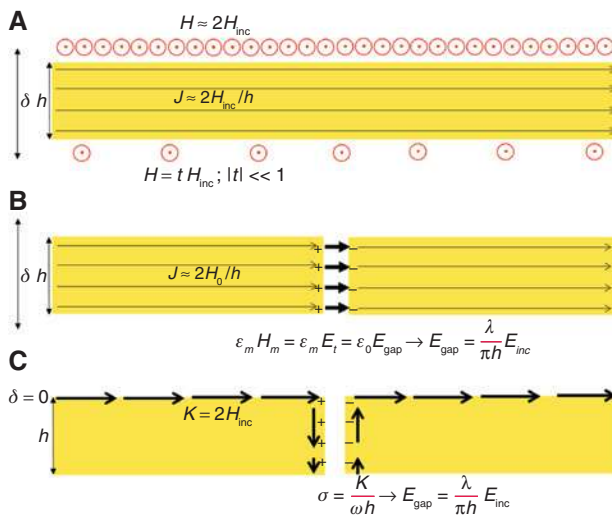
Figure 5: Field enhancement in thin and thick conducting films. (A) Magnetic field of light and current density near the thin film is represented in red, where THz impinges to the plane. The magnetic field is approximately twice at the incident surface (up) and much smaller at the transmission side (bottom). (B) Obtained displacement current and E_{gap} around the narrow gap. (C) Displacement current and E_{gap} at films much thicker than the skin depth.

where ε_∞ is the high-frequency dielectric constant of the metal and γ is the Drude damping constant (Figure 5B). The physics of the conductivity independence of the *FE* is then clear: better conductivity makes the field inside the metal weaker, which is compensated by the higher dielectric constant of the metal when applying the displacement current boundary condition. Equation (1) can be analytically extended into a completely different regime, for samples much thicker than the skin depth (Figure 5C); for this regime, we assume that current flows only at the surface with surface current density $K = 2H_{inc}$, and terminates at the exit side of the gap, dumping charges along the way, as shown in Figure 6. Interestingly, J_x component at the metal surface in the gap, shown in Figure 6C, is kept nearly constant, while J_z (Figure 6B) is not. This implies that the accumulated surface charge is evenly distributed over the metal surface, giving rise to constant E_x field in the gap. The continuity equation demands the surface charge density being $\sigma = \frac{K}{\omega h}$, from which $E_{gap} = \frac{\lambda}{\pi h} E_{inc}$ follows.

Aforementioned *FE* with thin ($w \sim h < \delta$) and thick ($w < \delta < h$) narrow gaps, together with wide gaps ($\delta, h < w$), are discussed in a recent paper [76]. Shown in Figure 7A are numerically calculated current distributions with narrow (1.5 nm) and wide (200 nm) gaps in 150-nm-thick gold films, and corresponding schematics for charge distributions are shown in Figure 7B. For the wider gap, charges are not mostly accumulated at the metal edges in the gap but are spread over the surface outside the gap. This consequently reduces the *FE*. For the narrower gap, most charges are accumulated at the metal edge in the gap, giving rise to stronger *FE*. However, we stress that when the aspect ratio w/h is sufficiently small ($w/h \ll 1$), the charge distribution becomes insensitive to the gap size, so that the *FE* will exhibit saturating behavior with decreasing w. Also, $1/h$ dependence of *FE* in narrow gap is well demonstrated (Figure 7C).

Having established a simple *FE* formulae for thin and thick samples limits, we proceed to include the very thin-regime, where t can no longer assumed to be $\ll 1$. Applying Ampere's law, we obtain $1 + r - t = \frac{\sigma_m t h}{\varepsilon_0 c}$. Applying energy conservation including Ohmic loss, we arrive at $1 = r^2 + t^2 + \frac{\sigma_m t^2 h}{\varepsilon_0 c}$. Solving these two, we get

$$FE = \frac{\frac{\lambda}{\pi h}}{1 + \frac{h_0}{h}}, \qquad (6)$$

with h_0 given by Eq. (3); Eq. (6) can now be applied to all three regimes of thicknesses.
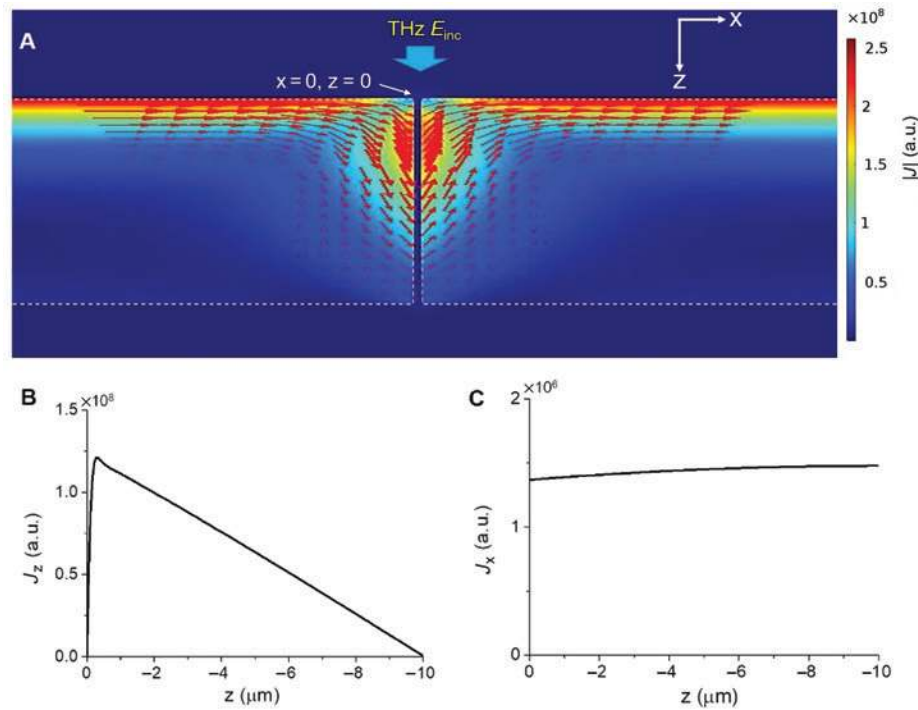
Figure 6: Field enhancement with thick slit.
(A) Numerically calculated map, using the COMSOL software, of the current density with thick slit in freestanding gold, showing "dumping the charge". 0.5 THz light is incident from the top side onto the gap of $w=10$ nm and $h=10$ μm. Metal surfaces are denoted by white dashed lines. Cross-cut profiles of (B) J_z and (C) J_x along the left metal edge in the gap [from (0, 0) to (0, $-h$)] are present.
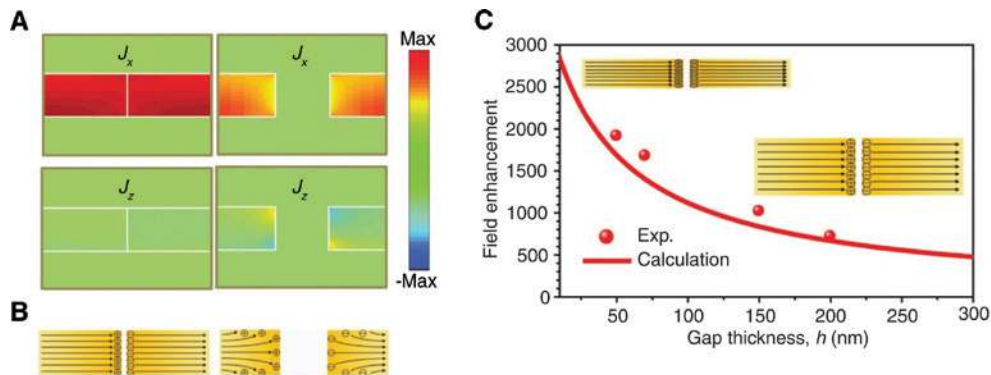

Figure 7: w/h-dependent field enhancement.
(A) Numerically calculated maps of induced current J in thin gold films. Here, $h=150$ nm and $w=1.5$ nm (left) and 200 nm (right). 0.3 THz incident light is considered. (B) Schematics of induced current and accumulated charges for narrow ($w \ll h$) and wide ($w \sim h$) gaps. (C) Experimentally measured and analytically calculated FE of 0.3 THz field in a 5 nm gap with varying thickness h. Inset figures illustrate higher surface charge density in a thinner gap, while total accumulated charge is independent of the thickness. Note that FE is modified from Eq. (1) due to the substrate effect. This figure is reproduced from Ref. [76].

To confirm that Eq. (6) gives a reasonably good description of the FE over many orders of magnitudes of conductivity, we plot, in Figure 8A, finite-difference-time-domain (FDTD) calculations (solid red line) for a 50-nm-thick film with 1 nm air gap varying conductivity over five orders of magnitudes. We also plot the FE of Eq. (6) (dash-dot line), showing good agreements. While the metal film in Figure 8A belongs to a very thin to thin regime, the $h=1000$ nm case shown in Figure 8B certainly belongs to the thick regime for $\sigma_m \geq 10^6$ Ω^{-1}m^{-1}; skin depth at 1 THz is 500 nm for a conductivity of $\sigma_m = 10^6$ Ω^{-1}m^{-1}.

Next, we consider the effects of a substrate. Assuming an infinitely thick substrate and applying energy conservation and Ampere's law, it is straightforward to show that
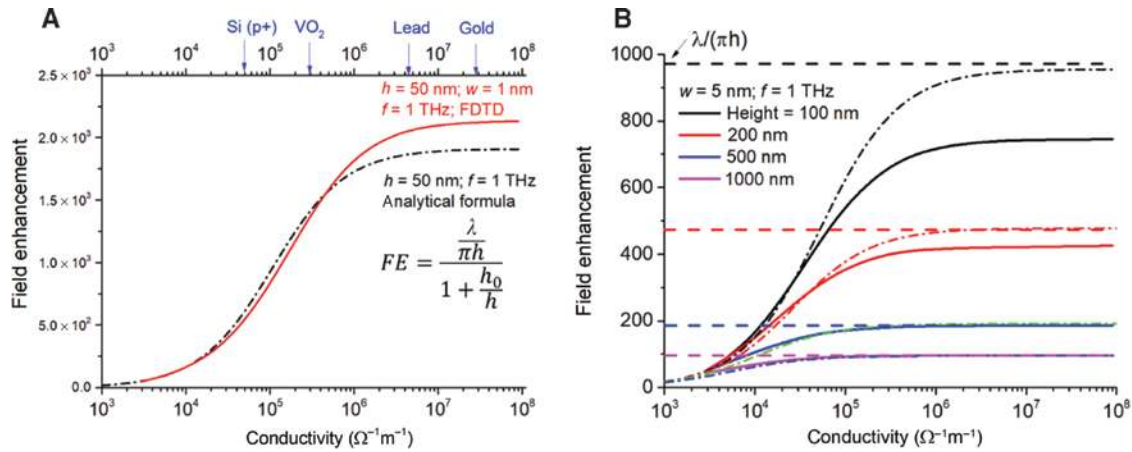
Figure 8: Field enhancement with varying conductivity of metal.
(A) Field enhancement for a 1-nm-wide gap in 50-nm-hick film at 1 THz is plotted in terms of conductivity, calculated by FDTD and analytical formula. In particular, typical conductivities of a heavily doped Si (p+), VO$_2$, lead, and gold cases are denoted in blue arrows. (B) Enhancement factors for 5-nm-wide gaps in several films with thickness of 100, 200, 500, and 1000 nm at 1 THz are plotted in terms of conductivity.

$$FE = \frac{\dfrac{\lambda}{\pi h}}{1 + \dfrac{h_0}{h}\dfrac{n_s + 1}{2}}, \qquad (7)$$

where n_s is the index of refraction of the substrate and the electromagnetic field is incident from the air side. In obtaining Eq. (7), as before, it has been assumed that the current flows straight into the gap. However, even for the high aspect ratio gaps, the asymmetry caused by the substrate would bend the current flow, resulting in loss of FE.

Although the result of FE from our model is surprisingly simple, we would like to emphasize that the same FE rule can be obtained from more rigorous analytic theory. Coupled mode theory with single-mode approximation, dealing with boundary conditions of Maxwell's theory with single quantized waveguide mode in the gap, provides that the FE by a gap in very good conductor on the substrate can be written as [177]

$$FE = \left| \frac{4}{e^{-ik_0 h}(1 + W_s)(1 + W_0) - e^{ik_0 h}(1 - W_s)(1 - W_0)} \right|, \qquad (8)$$

where W_0 and W_s are the light-gap coupling factors defined by

$$W_0 \equiv k_0 \frac{1}{2w} \int_0^w dx \int_0^w dx' H_0^{(1)}(k_0 \sqrt{(x - x')^2})$$

and

$$W_s \equiv n_s^2 k_0 \frac{1}{2w} \int_0^w dx \int_0^w dx' H_0^{(1)}(n_s k_0 \sqrt{(x - x')^2}), \qquad (9)$$

with $H_0^{(1)}$ being the Hankel function of the first kind. For a narrow gap ($w \ll \lambda$), the coupling factors can be approximated as

$$W_{0,s} \approx n_{0,s}^2 k_0 w (2i\ln(n_{0,s} w k_0 / 2) + 2i\gamma_E - 3i + \pi) / 4\pi, \qquad (10)$$

where $n_0 = 1$ and γ_E is the Euler constant. The explicit form of FE is somewhat complicated, but clearly, a further simplification can be made by the fact that the coupling factor approaches zero as the gap size approaches a deep subwavelength regime. Interestingly, one can readily find from Eqs. (8) and (10) that, in the limit of $w \ll h \ll \lambda$, regardless of the substrate, Eq. (8) can be reduced to

$$FE \approx \frac{\lambda}{\pi h}, \qquad (11)$$

which perfectly coincides with our main result of FE in Eqs. (1) and (7) with $h_0 \ll h$. Even though the FE in the ultimate limit is the same with the free-standing case, however, we point out that the FE with a substrate will be generally lower. This is related to the nature of logarithmic dependency of the coupling factor in Eq. (10), which yields, in the presence of the substrate, slower vanishing of the coupling factor as w approaches zero. We point out that the physical account of the reduced FE can be found from the impedance mismatch at the air-substrate interface in the gap that naturally leads to reduction of the tangential component of the electric field near the surface [147].

It should be also noted that, for periodic arrays of slit, FE is limited by the periodicity especially when the
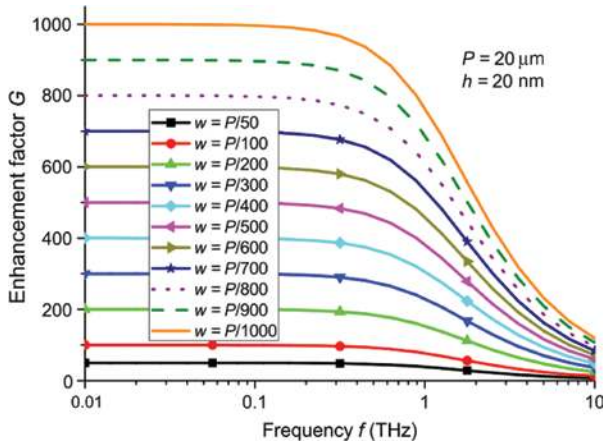
Figure 9: Field enhancement in periodic arrays of slit, clearly exhibiting that the enhancement factor is strongly limited by the subwavelength period P.
This figure is reproduced from Ref. [89].

period is in subwavelength scale, as shown in Figure 9 [89]. This is an intuitive result in that the enhancement is basically related to the funneling of electromagnetic energy and that periodic slits share available energy from the incident wave, giving rise to reduced *FE* in each slit.

Another relevant physics that should be addressed is the enhancement of the magnetic field with metal nanowire, a Babinet complementary structure of nanogap (shown in Figure 10). Although the strict Babinet principle is applicable only to structures of an infinitesimally thin perfect electric conductor, Koo et al. [68] theoretically demonstrated that a qualitative prediction of *FE* in a complementary structure can be doable from a metal of finite thickness and conductivity.

2.2 Estimation of the field enhancement from far-field measurements: Kirchhoff integral method

Experimental verification of the huge *FE* by the direct measurement of near-field is a technically challenging issue because of the limited resolution of the near-field imaging, restricted by the spot size of optical probe beam, which is usually in a few micrometers [178–185]. To improve this issue, a more elaborately complemented scheme is introduced, of which a main idea is based on the Kirchhoff diffraction theory [186, 187] that provides approximated relationship between the near-field information and the signal in sufficiently far distance [69, 188]. A typical experimental setup utilizing the Kirchhoff method to extract the THz *FE* in the gap is illustrated in Figure 11. This utilizes the transmitted signal through the "normalizing aperture" as reference signal.

The scheme starts from the Kirchhoff integral expression of far-field electric field diffracted by an aperture,

$$\vec{E}(\vec{r}) = \frac{ie^{ikr}}{2\pi r}\vec{k} \times \int_A \hat{n} \times \vec{E}(\vec{r}')e^{-i\vec{k}\cdot\vec{r}'}da', \tag{12}$$

where r is the distance from the origin, i.e. center of the aperture; A is the aperture area; and $\hat{n}$ is the normal vector to surface A [188]. We note that Eq. (12) can be significantly simplified if the measurement is performed at the diffraction center, $(0, 0, z)$ with $z \gg \lambda$. For a simple instance, assume that we measure a far-field signal from a $w \times L$-sized slit together with the normalizing aperture of same length L but different width w_a. The far-field signal E_{far}^s from the slit at $(0, 0, z)$ can be written as
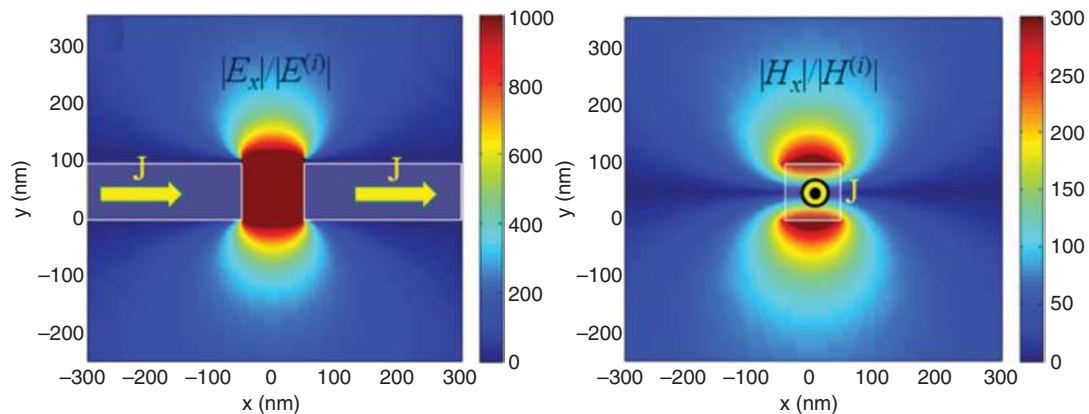
Figure 10: FDTD-calculated electric (left) and magnetic (right) field enhancements with nanogap and nanorod, respectively (gold, $h = 100$ nm, $w = 100$ nm).
This figure is reproduced from Ref. [68].
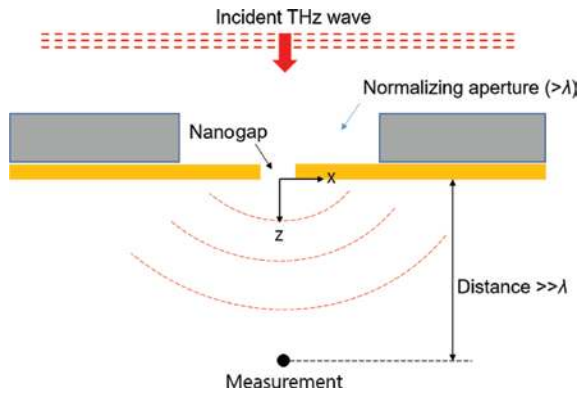
Figure 11: Schematic for far-field measurement of THz field passing through a gap in metal.
Near-field enhancement can be estimated quantitatively by using the Kirchhoff integral method.

$$E_{far}^s = \frac{e^{ikz}}{i\lambda z} \int_0^w \int_0^L E_{near}^s \, dx \, dy = \frac{e^{ikz}}{i\lambda z} \langle E_{near}^s \rangle wL, \qquad (13)$$

where $E_{near}^s(x, y)$ and $\langle E_{near}^s \rangle$ are the electric field at the aperture-air boundary ($z=0$) and its averaging over the aperture area A, respectively. In the same manner, the far-field signal from the normalizing aperture can be expressed as

$$E_{far}^a = \frac{e^{ikz}}{i\lambda z} \int_0^{w_a} \int_0^L E_{near}^a \, dx \, dy = \frac{e^{ikz}}{i\lambda z} \langle E_{near}^a \rangle w_a L. \qquad (14)$$

Equations (13) and (14) give rise to

$$\frac{|E_{far}^s|}{|E_{far}^a|} = \frac{|\langle E_{near}^s \rangle|}{|\langle E_{near}^a \rangle|} \frac{w}{w_a} = \frac{|\langle E_{near}^s \rangle|}{|\langle E_{near}^a \rangle|} \beta, \; \beta \equiv \frac{w}{w_a}. \qquad (15)$$

This reveals that the ratio of far-field signals, directly measurable quantities, is related to that of the *FE*s, introducing the scale factor β given by the ratio of w and w_a. Here, in the limit of $w_a > \lambda$, one can find that *FE* by the reference aperture is close to 1, giving rise to $|\langle E_{near}^a \rangle| \approx |E_{inc}|$, where E_{inc} is the amplitude of incident field. This enables a further approximation of Eq. (15), implying that *FE* can be determined exclusively by quantities measurable in far-field:

$$FE \equiv \frac{|\langle E_{near}^s \rangle|}{|E_{inc}|} \approx \frac{1}{\beta} \frac{|E_{far}^s|}{|E_{far}^a|} \qquad (16)$$

Despite its simple expression, we stress that Eq. (16) was successfully used in various THz experimental studies to estimate *FE* with reasonable accuracy in comparison with the theoretical predictions [69].

In the presence of the substrate, the *FE* can be also estimated by the same scheme, taking into account of the transmission of waves at the interfaces of substrate. At first, as shown in Figure 12, consider the far-field measurement at the substrate side with incident THz wave impinging upon the metal from the top side. If the thickness of the substrate is sufficiently thick, the transmission amplitude of the incident THz waves through the substrate-only sample, E_{sub}, can be approximated by the direct transmission with ignoring the multiple reflection effect. That is, $E_{sub} \approx \frac{4n_s}{(n_s+1)^2} E_{inc}$. Then, the far-field transmission amplitude normalized by E_{sub} can be written as

$$|t| \equiv \frac{|E_{far}^s|}{|E_{sub}|} \approx \frac{|E_{far}^a|}{|E_{inc}|} \frac{\beta \frac{2n_s}{1+n_s} |\langle E_{near}^s \rangle|}{\frac{4n_s}{(n_s+1)^2}|E_{inc}|} = \beta \frac{|E_{far}^a|}{|E_{inc}|} \frac{2}{1+n_s} FE. \qquad (17)$$

Here, we used the result of Eq. (16). Since t is an experimentally measurable quantity, Eq. (17) says that *FE* with substrate sample can be also quantitatively estimated from the far-field signal by using the Kirchhoff integral method: $FE \approx \frac{1+n_s}{2\beta} \frac{|E_{inc}|}{|E_{far}^a|} |t|$.

For the reversed case, i.e. far-field measurement at the top side with incident THz wave impinging from the substrate side, the same scheme can be applied. What is different is that, in that case, the near-field signal radiates to the far-field freely without disturbance by the substrate. Therefore, Eq. (17) for the reversed measurement can be rewritten as

$$|t| \equiv \frac{|E_{far}^s|}{|E_{sub}|} \approx \frac{|E_{far}^a|}{|E_{inc}|} \frac{\beta |\langle E_{near}^s \rangle|}{\frac{4n_s}{(n_s+1)^2}|E_{inc}|} = \beta \frac{|E_{far}^a|}{|E_{inc}|} \frac{(n_s+1)^2}{4n_s} FE. \qquad (18)$$
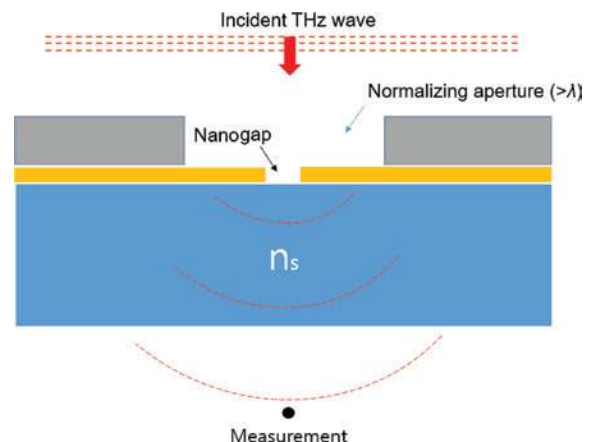
Figure 12: Schematics for the Kirchhoff method with substrate.

Interestingly, for the reversed measurement, it is better to just get the *FE* without using the substrate normalization. Then, Eq. (18) will be simply be $FE \approx \frac{1}{\beta} \frac{|E_{inc}|}{|E_{far}^a|}|t'|$, where t' is the transmission amplitude without going through the substrate normalization process.

2.3 Resonant versus nonresonant field enhancement

What we have discussed so far is basically nonresonant field enabled by the funneling process of THz waves through the gap, which is also related to the "capacitive enhancement". In contrast to such nonresonant *FE*, it is also extensively discussed that two-dimensional apertures such as circular or rectangular holes can support resonant *FE* when certain resonance conditions are met. In terms of strong *FE*, a rectangular hole, also known as slot antenna, is practically more suitable than other types of holes. This is because of the nature of resonance condition that usually requires a geometric size of the hole to be in wavelength-scale. A slot antenna having an ultrahigh aspect ratio of width w and length l (i.e. $w/l \ll 1$) can utilize resonant light-slot coupling together with capacitive enhancement, maximizing the *FE*.

There have been extensive investigations to obtain quantitatively accurate *FE* by single slots in metal [69, 90, 91, 189, 190]. The description of *FE* is shown to be also quite simple. However, compared to the single-slit case, its behavior is completely different. Analytic calculation based on the coupled-mode theory predicts that the resonant *FE* by a single slot of width w and length l (shown in Figure 13) is [90, 177]

$$FE_{res} \approx \frac{3l}{2w}\sin\left(\frac{\pi x}{l}\right), \tag{19}$$

where the resonance condition is simply given by

$$\lambda_{res} \approx 2l. \tag{20}$$

In Eq. (19), x varies from 0 to w. By taking average of the *FE* over the slot area, we have

$$\langle FE_{res}\rangle \equiv \frac{1}{wl}\int_0^w\int_0^l FE_{res}\,dxdy = \frac{3l}{\pi w} = \frac{3}{2\pi}\frac{\lambda_{res}}{w}. \tag{21}$$

It should be noted that retrieval of *FE* from the far-field measurement by using the discussed Kirchhoff integral method is related to Eq. (21), not Eq. (19). It is interesting to see that the resonant *FE* by single slot is given by the aspect ratio of width and length. Clearly, compared to the nonresonant $FE = \frac{\lambda}{\pi h}$, Eq. (21) shows distinctive behaviors.

This simplified *FE* can be broadly applied to the range of micron gaps to nanogaps. Enhanced electromagnetic field through subwavelength gaps have been intensively explored both theoretically and experimentally over ultra-broadband wavelength regime covering microwave [191, 192], THz [98, 193–195], IR [196, 197], and visible regime [198, 199]. Especially subwavelength photonics has been focused on THz frequencies (0.1–10 THz, 0.03–3 mm), having taken advantage of their relatively large aspect ratio between the wavelengths and structure scales, in turn providing a colossal *FE* effect. The studies, unavoidably, have strongly relied on the development of the state-of-the-art fabrication technologies for engineering small structures, which have been greatly advanced in the past decade [200–202]. As an earlier work on THz metallic gap structures, micrometer scale rectangular hole arrays were prepared using femtosecond laser machining technique, which guarantees wavelength length scale
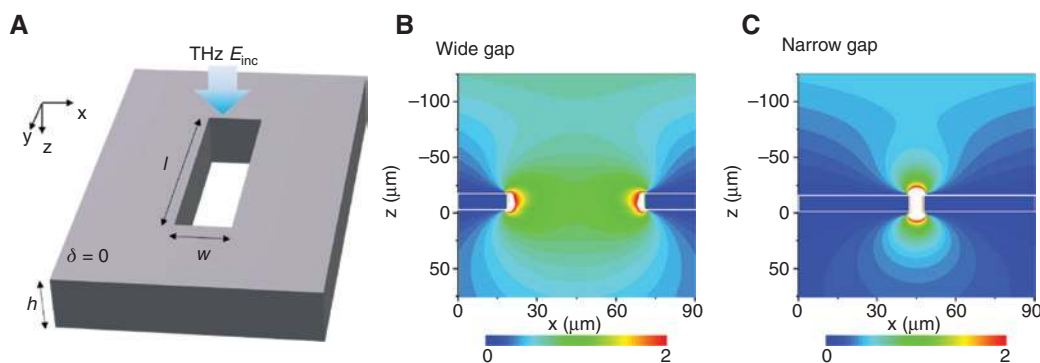
Figure 13: Field enhancement in a rectangle slot.
(A) Schematic of single rectangular hole punctured onto a metallic thin film with a length *l* and a width *w* and a thickness of *h* is irradiated by THz incidence. Transmitted THz field distributions for wide gap (B) and narrow gap (C) calculated by FDTD [184].

perforation onto metal thin film (typically several tens to hundreds μm) and somewhat less [203, 204], as shown in Figure 13A.

The resonance can be tuned by changing the length of the rectangular holes, *l*. Then, as expected, the confined THz field near the gap and *FE* value increase with decreasing of the hole width (Figure 13B, C and Figure 14). The *FE* value is independent of the thickness *h*. Although we discussed the resonant *FE* only with a single slot case mostly so far, we note that a single slit can also support two different types of resonances: Fabry-Perot-type resonance that appears when the thickness of the slit is comparable to the half-wavelength [64, 205] and the so-called fractional resonance from an ultrathin single slit filled with negative permittivity media [191].

# 3 THz nonlinearity in few- and subnanometer gaps by quantum electron tunneling

Classical theory of electromagnetism, describing microscopic light-matter interactions in terms of effective dielectric constant, predicts the THz *FE* by nanogaps in metals, in the form of electric field distribution obtained as a solution of the required boundary conditions at interfaces of metal and free-space [206–210]. The predicted result is quantitatively accurate especially when the gap size is a few nanometers or larger [88, 89, 156], and the enhancement by an infinitely-long nanogap is shown to

Figure 14: Normalize-to-area light transmission through single rectangular slot in perfect electric conductor plate, implying that the total transmission is almost independent of the width *w*.
Here, $\lambda_c = 2l$ is the resonance condition. This figure is reproduced from Ref. [48].

increase with decreasing gap size up to the enhancement factor, $\frac{\lambda}{\pi h}$. It is also confirmed experimentally that this behavior is still valid even when the gap approaches the regime of the sub-skin-depth [69].

One immediate question that arises here is whether this increasing behavior continues to the subnanometer regime. Considering the zero-gap limit in which there is no *FE* and that gap-size-dependent *FE* changes continuously with varying gap, one can presume that there should be a critical turning point of the gap size at which the near-field strength eventually starts decreasing with even narrower gap. Classical theory predicts that, in the perfect electric conductor approximation widely used in the study of THz wave interaction with metals, there is no such decrease in the *FE*. Exceptionally, the decreased *FE* with finite conducting metal is mainly due to the evanescent decay of the fundamental slit waveguide mode that becomes more pronounced with narrower gap in lossy material [91, 148]. Recently, experimental and theoretical studies demonstrated that when the gap size approaches a few nanometers or Angstrom regimens, *FE* can be strongly modified and the classical theory cannot provide a quantitative understanding without taking into account quantum effects [86, 167, 211–215]. In this regime, numerical schemes such as conventional finite-element method (FEM) and FDTD based on far-field dielectric function of the material also should have an implementation of the quantum effect for accurate calculations of *FE*.

There are two major quantum effects that come into play when the gap size approaches the nanometer or Angstrom regime. Nonlocal plasmon response [216–230] is an extensively discussed, quantum-mechanical counterpart of the classical local response theory, giving rise to a suppression of the local *FE* through a modification of effective boundaries of materials within the Fermi-wavelength scale (nm to Angstrom). We note that the nonlocal effect can be directly applied to the FEM and FDTD schemes by adapting quantum-corrected dielectric functions of the materials. It should be also noted that, in some extent, the nonlocal effect is related to the Landau plasmon damping [231–233] that results in additional suppression of the plasmonic electric field in the proximity of metals [234].

In this section, we discuss the other important quantum effect, the electron tunneling [235–238], through a potential barrier of nanogap at THz frequencies [76, 80, 86], incorporating recent studies. In the point of view of electrons, a gap in a metal plate can be assumed as a tunnel junction [239, 240], as shown in Figure 15A. Usually, the gap size for an efficient electron tunneling needs to be subnanometer for typical potential barriers of the gap, a
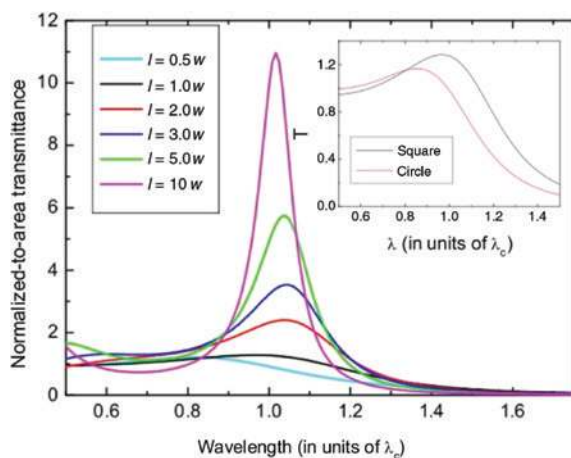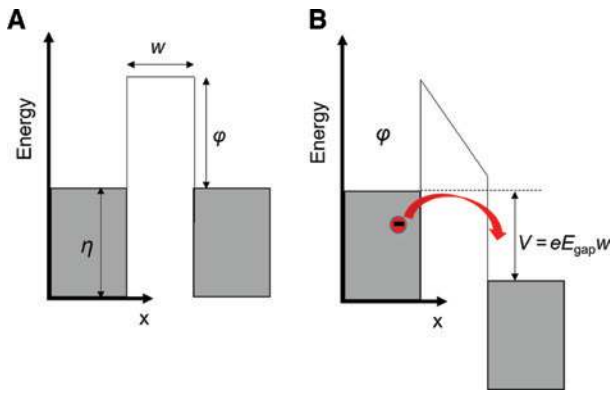
Figure 15: Electron tunneling through a nanogap.
Tunnel junction (A) without and (B) with strong electric field in the gap, E_{gap}. Here, η is the Fermi level and φ is the barrier height.

few eV. As shown in Figure 15B, an intense electric field is required to pull down the barrier for tunneling. We will see that, thanks to the ability of the nanogap in metal to capture the intensive THz field, the THz quantum tunneling and consequent strong nonlinear behavior result both in subnanometer [79, 80, 85] and even in super-nanometer gaps [76, 86].

3.1 Fabrication of wafer-scale nanogap arrays

A challenging issue for the experimental studies on THz plasmonics with few- or subnanometer gap is sample fabrication because of extremely high ratio of photon wavelength and gap size. To have a reliable THz field interaction with nanogap and consequent plasmonic behaviors such as giant local *FE* and nonlinearity, the length of the gap should be at least in the scale of photon wavelength. Therefore, in pursuit of sufficiently intense far-field signal, the sample should cover several mm² area with nanogap
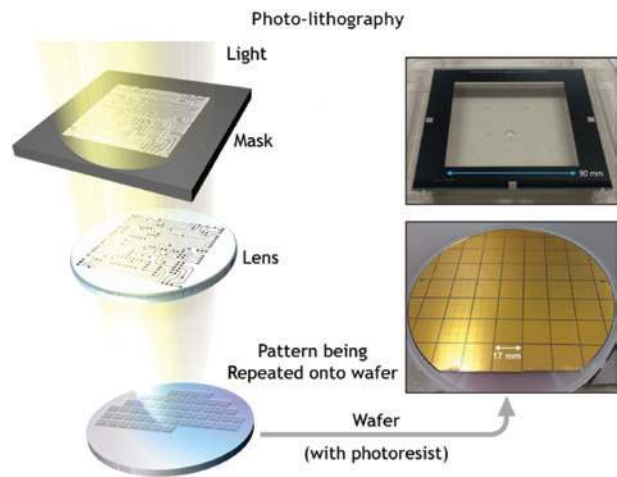
Figure 16: High-resolution and high-throughput technique for nanogap array fabrication.

arrays of ultrahigh aspect ratio. To realize such large-area sample with high-resolution patterning, various recipes have been introduced, e.g. fs-laser machining for micro-scale punctured structures [64, 241, 242], focused ion beam [243, 244], e-beam lithography [245, 246], and photolithography techniques [125, 247, 248] for metamaterial structures and, finally, atomic layer deposition (ALD) for atomic-scale gap structures [75, 193, 249, 250]. For nanoscale gap structures, photolithography can be considered as a promising fabrication method for mass production at the same time, as shown in Figure 16. The stepping method using patterned mask guarantees several hundreds of nanometers in gap width with hundreds of microns in gap length, required for resonant enhancement of THz field (Figures 13 and 14). Also, by varying the length of the gap, l, one can obtain frequency tunable THz resonators (Figure 17A), showing a clear relationship between l and the fundamental resonance frequency, f_{res} (Figure 17B).
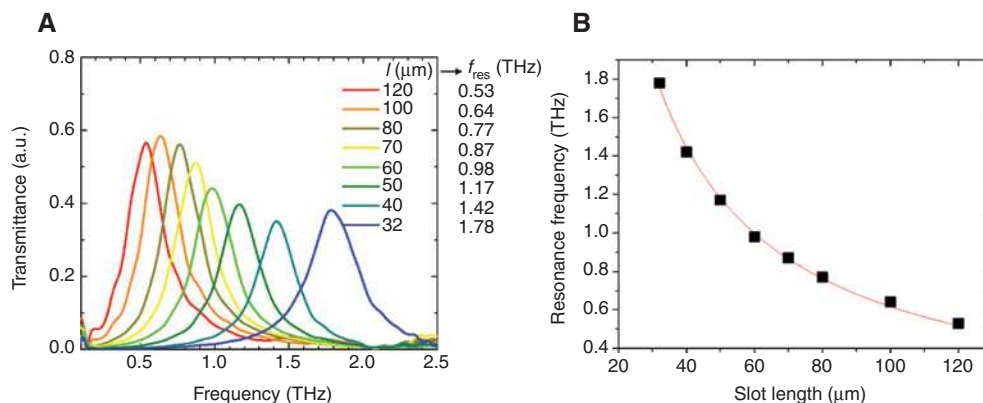
**Figure 17:** Transmittance with varying slot length.
(A) Measured THz transmittances for various slot arrays. (B) The resonance frequencies for different slot arrays are plotted in terms of the slot length.

For the ultimately small subnanogaps, on the one hand, a spacer deposition method [75, 251] provided strong reliability in terms of preventing collapsing of the gap and controllability of precise thickness, enabling a 1-nm gap uniformly formed with several 100 microns length.

Figure 18 illustrates the sample fabrication scheme introduced by Jeong et al. [102], an improved version of the previously introduced scheme by Chen et al. [75] (Figure 19). Firstly, on the 3 nm chromium (Cr)/100 nm Au/sapphire substrate, 30 nm Cr and 150 nm aluminum Al layers are patterned by using a standard photolithography and liftoff process. This double layer is a sacrificial layer that will be used for removing excess metals and making the structure planar. Then, because Al is resistant to ion beam, ion milling is applied to remove exposed Au area while Au underneath the Al/Cr layer is sustained. After that, the ALD of aluminum oxide (Al_2O_3) is applied to form a uniform clad on the whole structure with nanometer-scale thickness. After the deposition of a second Au layer with adhesive Cr layer, Al/Cr wet etching is applied to remove the overhanging Au and Al layers.

In the above recipe, the nanogap is defined by the ALD of Al_2O_3, providing controllability in nanometer accuracy. Based on spacer deposition and filling schemes, and by adding a step of sacrificial layer, this method provides high-throughput fabrication of nanogaps with an ultrahigh aspect ratio.
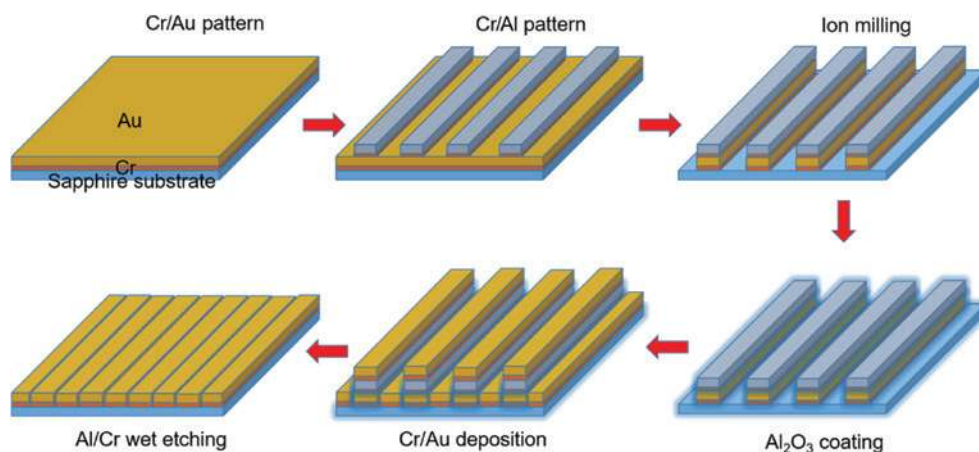
Figure 18: High-throughput fabrication of arrays of nanoslits with ultrahigh aspect ratio introduced by Jeong et al. [102].
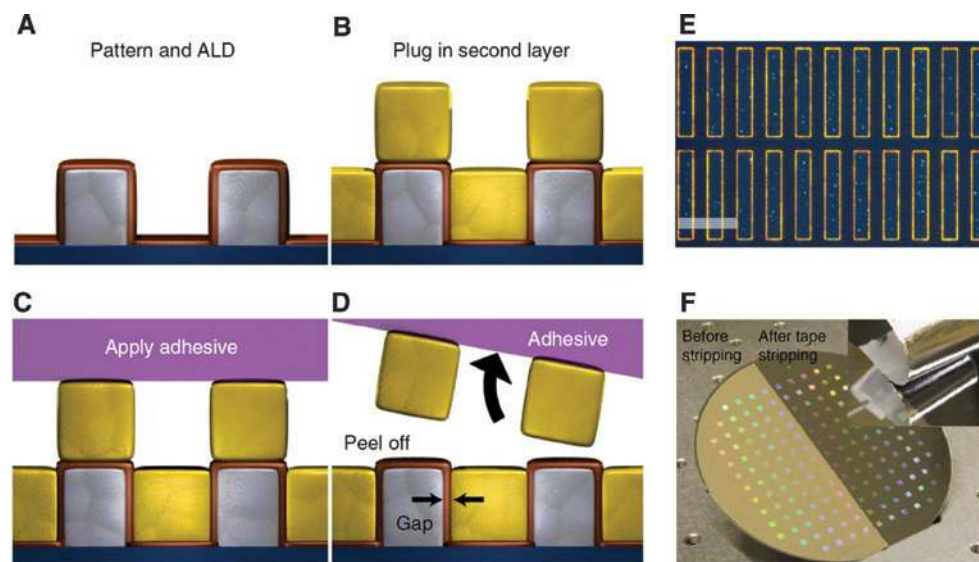
Figure 19: Wafer-scale atomic layer lithography.
(A) A patterned substrate coated with a thin Al_2O_3 by using ALD. (B) Additional metal evaporation to plug the second layer. (C, D) Removal of the excess metal by using an adhesive. (E) Optical micrograph of 5-nm gaps in silver. White scale bar indicates 0.2 mm. (F) Half of a Si wafer planarized by using an adhesive. This figure is reproduced from Ref. [75].
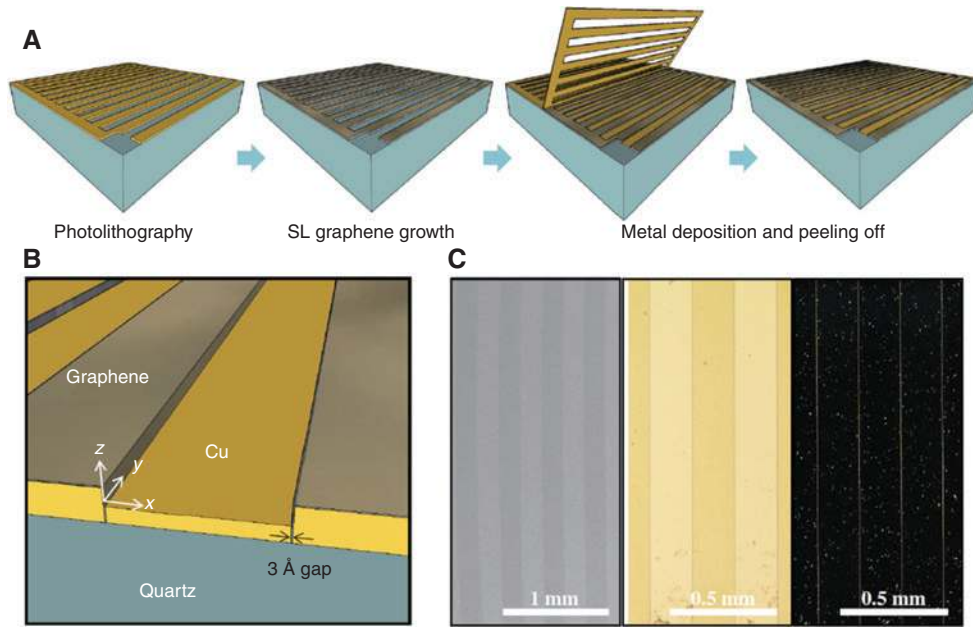
Figure 20: Fabrication of vertically oriented graphene spacer in Cu-single layer graphene (SLG)-Cu composite.
(A) Schematic of the fabrication procedure. (B) Cross-sectional image of Cu-SLG-Cu array. (C) Top views of SEM (left), reflection type (center), and dark field scattering (right) optical microscope images. This figure is reproduced from Ref. [80].

Shown in Figure 20 is fabrication of Angstrom gaps introduced by Bahk et al. [80]. First, on a patterned 300-nm-thick Cu film on a quartz substrate, a single-layer graphene (SLG) is seamlessly grown to cover the sidewalls. Then, an additional thinner Cu layer is deposited on the same sample by thermal evaporation. Finally, the second Cu layer is selectively peeled off by using an adhesive tape: the final result is Cu-SLG-Cu composite as shown in Figure 20C.

## 3.2 Nonlinear THz response by light-induced electron tunneling through nano- and Angstrom-sized gaps

A basic strategy to realize the THz nonlinearity is utilizing deep subwavelength gap to induce huge electric field that consequently pulls down the barrier in the tunnel junction by the potential energy $V = eE_{gap}w$, where e is the charge of electron, E_{gap} is the induced electric field in the gap, and w is the gap size. Since the electric field normal to the metal surface is related to the surface charge, E_{gap} can be quantitatively determined by the accumulated surface charges at the two metal walls in the gap. This implies that, once electron tunneling occurs, a further charge accumulation by the incident THz field is limited and the FE will be reduced. Also, because the pulling down of the potential barrier increases with stronger E_{gap}, naturally more intense THz field leads to more electron tunneling through the potential barrier, giving rise to more pronounced nonlinear responses in local electric FE and transmission of THz waves through the gap.

As discussed above, THz nonlinear behaviors through the nanogaps have been introduced by recent experimental studies [86, 252, 253]. In Ref. [86], arrays of nanogap are prepared based on the previously discussed ALD method with the sacrificial layer [75, 86]. An electron microscope image of the nanogap is shown in Figure 21A. Four different samples with selected gap sizes (1.5 nm, 2 nm, 5 nm, and 10 nm) are prepared to examine the THz nonlinearity depending on the tunneling probability. Shown in Figure 21B is the cross-section images of a 1.5-nm nanogap taken by a scanning electron microscope (top) and a scanning transmission electron micrograph (bottom). Note that the Al_2O_3 layer, presented in Figure 21B as a white area, defines the gap size, and its thickness, i.e. gap size, is controllable by the number of ALD cycles. The main result of this study is shown in Figure 21C. The THz transmission dependent on both E_{gap} and gap width clearly shows that the tunneling process works to reduce the THz transmission, corresponding to the reduced local electric field. Also, we note that reduced transmission in a nanogap with smaller width is more sensitive to an increase in E_{gap}, which is an intuitive result from that the smaller gap allows electron tunneling with higher probability. Nevertheless, it is clear that for the super-nano-gaps, what is most important is not the transient voltage applied to the gap so much as the electric field on the gap.
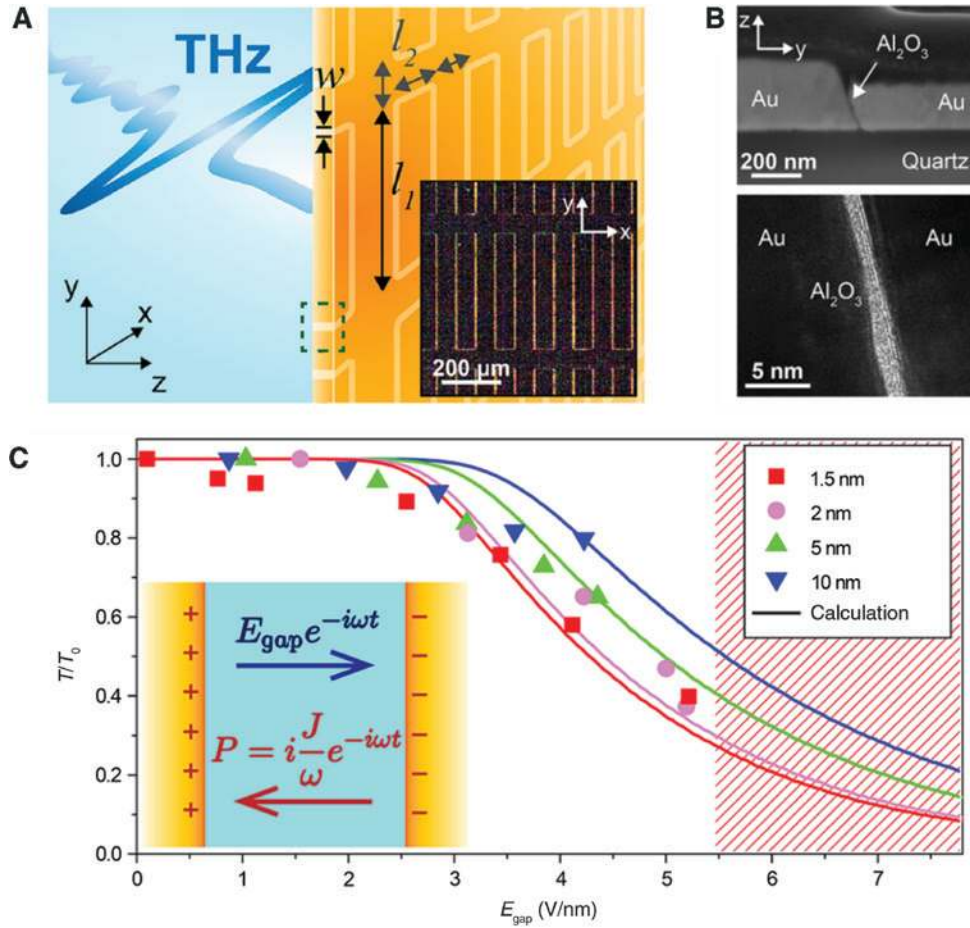
Figure 21: Nonlinearity in THz transmission through nanogaps.
(A) Optical micrograph image of arrays of nanoslot of 10 nm gap size. (B) Cross-section image of a 1.5-nm-wide gap from an SEM (top) and an STEM of the Al_2O_3 layer between gold (bottom). (C) THz transmittance with varying electric field amplitudes inside the gap. The dashed region (right) indicates where the gap is damaged by the induced electric field. This figure is reproduced from Ref. [86].

A nonlinear THz transmission can be quantitatively studied based on the dielectric response of the gap associated with the modal expansion method. This is an effective medium model in which the contribution of tunneling is interpreted as the transient modification of an effective dielectric function in the gap. As shown in Figure 21C, tunneling yields the tunneling current density, J, redistributing the induced surface charges near the gap. For a time-harmonic THz wave with angular frequency, ω, the polarization $P = i(J/\omega)\exp(-i\omega t)$ can be obtained, and consequently, the effective dielectric function ε can be described as

$$\mathrm{Im}\left(\frac{\varepsilon}{\varepsilon_0}\right) = \frac{J}{\varepsilon_0 \omega E_{\mathrm{gap}}}. \qquad (22)$$

The explicit form of the current density, J, dependent on both the gap size and the dielectric function of filling medium, i.e. Al_2O_3 in this case, can be evaluated by the image force model [254]. By applying Eq. (22) to the nanogap with a filling medium possessing effective dielectric function, the FE can be obtained in analytic ways that we discussed in Section 2. As shown in Figure 21C, the calculated results are in very good agreement with experimental results.

Recently, squeezing THz waves into much narrower gaps, Angstrom-size gaps, and consequent tunneling effect resulting in significant reduction of light transmission were demonstrated with the help of two-dimensional (2D) van der Waals (vdW) materials [80]. A heterostructure of 2D SLG and an effective vertically aligned 3 Å gap in copper layer, formed by Cu/1.5 Å gap/C/1.5 Å gap/Cu double vdW gaps of a 5 mm length, has revealed extreme THz nonlinearity with unprecedented 97% reduction of the transmittance through the gap (Figure 22). This self-limiting, gigantic optical nonlinearity is achieved by a massive THz funneling through Angstrom gaps, strongly pulling down the gap barrier and boosting the electron tunneling.
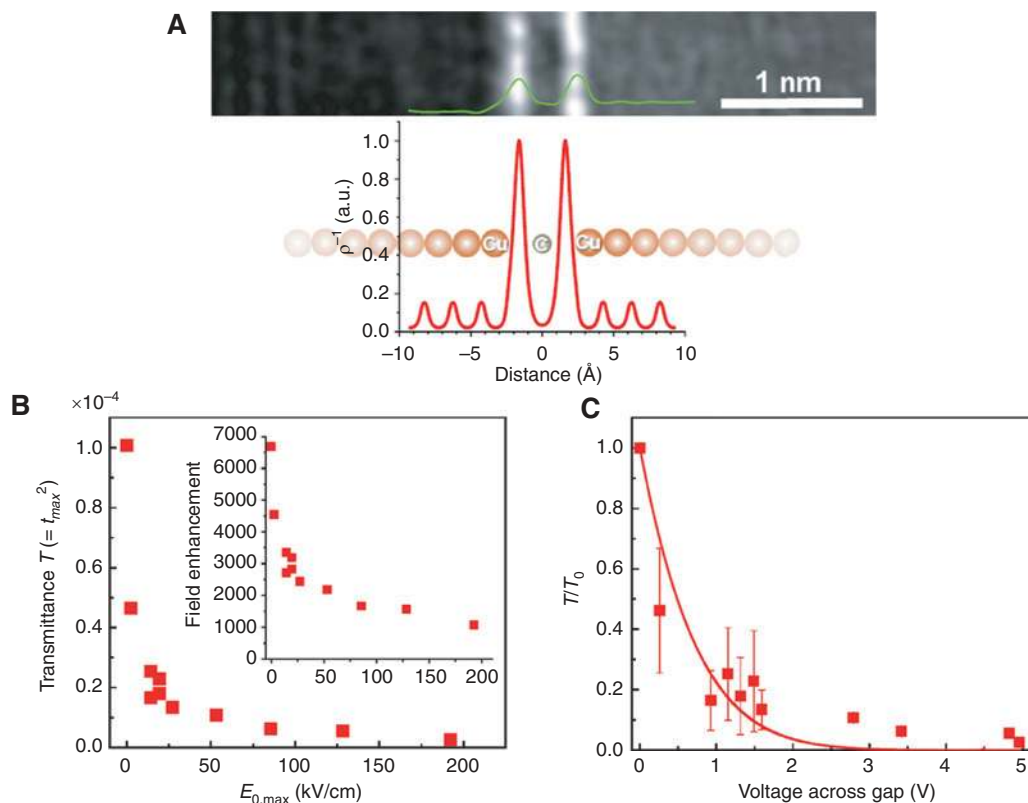
Figure 22: Nonlinearity in THz transmission through Angstrom-sized vDW gap.
(A) Cross-sectional TEM image of Cu-SLG-Cu composite (top). The green curve is vertically averaged line profile of the composite. The red curve (middle) denotes the plane-averaged inverse valence electron charge density. (B) Maximum normalized transmittance with varying incident THz field E_0. Inset represents retrieved FE calculated by using the Kirchhoff method. (C) Measured (dots) and calculated (curve) nonlinear optical response where T_0 is the transmittance without nonlinear response. This figure is reproduced from Ref. [80].

We note that the discussed THz quantum tunneling spans the boundaries of the study on quantum effects in microscopic light-matter interaction: down to the low frequency of 0.1 THz, up to strong field amplitudes of 5 V/nm, with barrier width from Angstrom to super-nanometer regimes.

4 Nanostructure-based absorber integrated terahertz sensor applications

Since many intramolecular and intermolecular vibration modes of molecules, including nucleobase [255–257], amino acid [258–261], and protein [262–264], exist at THz frequency range, THz technology has been considered a promising mean for detection and spectroscopy of such small biomaterials. Even bigger and more complex biological structures such as cell [265–268] and tissues [269, 270] can be explored with THz spectroscopic tools as well.

Unlike ultraviolet light or X-rays, the low photon energy of THz (1 THz = 4 meV) is an advantage to use because of noninvasiveness and nonionizing manner [271, 272]. Nevertheless, an extremely small absorption cross-section has limited widespread use in the THz regime. In most spectroscopic cases, chemical compound samples were prepared in closely packed pellet form to get reasonably big signal. Furthermore, bio or chemical samples in solution state have huge water absorption at the THz frequency, and thermal fluctuation at room temperature can hinder high-throughput applications. Sometimes, the experiments have been performed at a low temperature to rule out thermal fluctuation issues [273]. In this respect, recently advanced THz detection technologies assisted by micro-to-nano patterned (gap) structures can provide an excellent solution to these fundamental [103, 274–285]. Giant absorption cross-section enhancement of molecules inside nanogap structures will be discussed in this section showing a completely new type of label-free detection methods in room temperature. Examples of recent works will show that various type of samples are detectable even

in very low concentration, including chemicals, protein, microorganism, and even viruses.

4.1 Increased molecular absorption cross-section by THz nanogaps

Metal nanogap structures can enormously enhance and strongly localize the THz electric field at a hot spot, increasing the THz absorption coefficients of molecules [274]. Using a single nanogap structure in gold, it has been demonstrated that the molecular cross-section and absorption coefficient are enhanced by a factor of $E_{gap}/Z_0 H_{gap} \sim 10^3$, where H_{gap} is the magnetic field inside the gap. The origin of increased absorption coefficient is a strong asymmetry between THz electric and magnetic *FE*s: over a thousand times for the electric field, but in order of one for the magnetic field inside the gap. By considering the cross-section $\dfrac{dS}{dz} = -\sigma NS$ where dS is the Poynting vector absorbed between the points z and $z+dz$ along the path of a THz beam, N is the number of absorptive molecules per unit volume, and σ is the molecular absorption cross-section, molecular absorption can be calculated as follows: the Fermi Golden rule says that one molecule absorbs $\dfrac{2\pi}{\hbar}\mu^2 E^2 \rho(\hbar\omega_0)\hbar\omega_0$ (Joule per second), where μ is the electric dipole moment of the molecule, $\rho(\hbar\omega_0)$ is the density of states, and ω_0 and E are the resonant angular frequency and the local electric field of light, respectively. A volume, Adz (A is a surface area and dz is a differential thickness), can be defined, inside which the molecular absorption is occurring. By energy conservation, we have

$$[S(z) - S(z+dz)]A = (NAdz) \times \frac{2\pi}{\hbar}\mu^2 E^2 \rho(\hbar\omega_0)\hbar\omega_0$$

$$\frac{dS}{dz} = -N \times \frac{2\pi}{\hbar}\mu^2 E^2 \rho(\hbar\omega_0)\hbar\omega_0 \equiv -\sigma NS \qquad (23)$$

$$\sigma = \frac{2\pi}{\hbar}\mu^2 E^2 \rho(\hbar\omega_0)\frac{\hbar\omega_0}{S} = \frac{dS}{dz} = \frac{2\pi}{\hbar}\mu^2 \rho(\hbar\omega_0)\hbar\omega_0 \frac{E^2}{S}$$

The third line of Eq. (23) implies that the molecular absorption cross-section, σ, is sensitive to the electromagnetic environment of E^2/S, which greatly increases in the nanogap relative to the vacuum, owing to the asymmetric electromagnetic enhancements. A single nanogap with varying gap width from 50 nm to 5000 nm was used as a launching pad for strongly enhanced and localized THz field and a sensing hot spot at the same time. The first tested sample was an RDX (1,3,5-trinitroperhydro-1,3,5-trizine)

powder that has an absorption feature around 0.8 THz, attributed to a molecular conformation or a weak hydrogen bond between RDX molecules. Therefore, the sensing chip with a fundamental resonance at 0.87 THz was designed to selectively enhance the absorption frequency and used to detect RDX in a very low amount as shown in Figure 23.

The strongly increased molecular cross-section by $>10^3$ was translated into a colossal absorption coefficient of $\sim$170,000 cm^{-1}. Thereby, extremely small quantities about 40 ng (even 22 fg inside the gap) could be detected [260]. A theoretical model was also introduced to explain this and is in good agreement with a reference [286]. At this point, it should be noted that there are several critical parameters in designing the THz nanoslot antenna in terms of the target samples. First, the fundamental resonance frequency shift for the nanogap structures should be accounted for molecule detection. When bio and chemical compounds are filled inside the gap, their effective refractive index can significantly affect the measured THz spectrum. The resonance frequency can be determined by the following relation [90]: $f_{res} = \dfrac{c}{\lambda_{res}} = \dfrac{c}{\sqrt{2(n^2+1)}l}$, where l is the length of the gap and n is the real part of the complex refractive index. This means that, because the refractive index is dependent on the covered (drop-casted or filled) dielectric sample material, so is the shifting behavior of the resonance frequency [103, 275, 280]. Also, the gap width is a very important parameter related to the amount of the THz *FE* [188]. As discussed in the second section, a narrower gap yields a stronger THz *FE*, resulting in the increase in detection sensitivity. The gap-size-dependent detection sensitivity can be directly observed in the measurement of an extremely small amount of pesticides [287]. According to the measurements in Ref. [287], the observable minimum concentration level of targeted methomyl solution is determined by the gap size, and surprisingly, using 500 nm and 100 nm width gap antennas, 8 ppm and 10 ppb of methomyl at the measureable limit were detected, respectively. This observable limit value is essential for the label-free sensing [288], especially for extremely low concentration of chemical and biological residual substances.

4.2 THz nanogap sensor applications for chemical compound identification

As previously discussed, enhanced THz field by metallic nano structures can provide highly advanced sensing performance basically in label-free [289], noncontact,
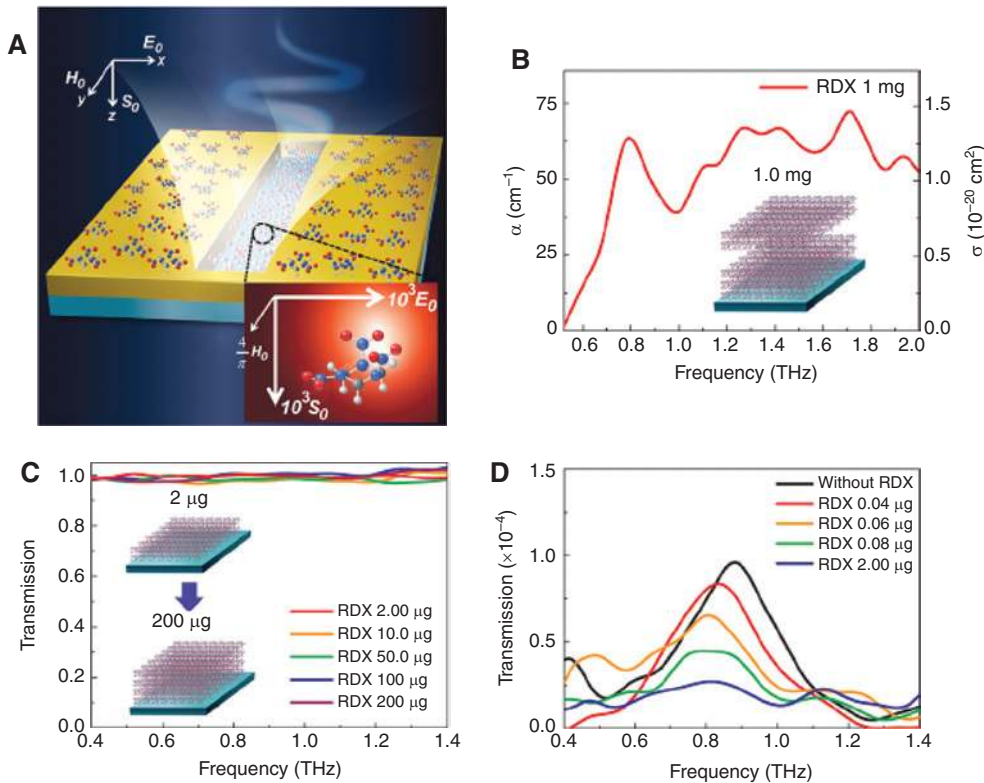
Figure 23: Interaction of molecules with THz nano antennas.
(A) Schematic of the enhanced absorption cross-section of RDX molecules inside a THz nanogap. (B) Absorption spectrum for 1 mg of RDX molecules onto the bare substrate. (C) Transmission spectra for RDX onto the substrate without nanogap. (D) Transmission spectra for a single THz nanoslot antenna without and with RDX ranging from 40 ng to 2 μg. This figure is reproduced from Ref. [274].

and noninvasive manners. THz optical characteristics of various biomaterials can be represented in terms of the dielectric response in the THz range. For example, the refractive indices for various saccharides can be extracted from the transmitted THz spectra in the range of 0.5–2.5 THz [290, 291]. Using the fast Fourier transform, the THz signal in time domain is converted to the amplitude and phase spectra in the frequency domain. Then the complex optical constants can be calculated with the waveforms for reference (typically void aperture) and target sample as a film (or pellet) form as follows:

$$E_s(\omega) = E_r(\omega) \cdot \exp\left(-\frac{d \cdot \alpha(\omega)}{2}\right) \cdot \exp\left(i\frac{2\pi}{\lambda}n(\omega)d\right), \quad (24)$$

where $E_s(\omega)$ is the amplitude of the transmitted signal through the sample and $E_r(\omega)$ is the amplitude of the input signal through empty space occupied with the film. $n(\omega)$ and $\alpha(\omega)$ are the real parts of the refractive index and absorption coefficient, respectively, and d is the thickness of the film. The power absorption extracted from the difference between the spectral amplitudes passing through the sample and reference is attributed to the imaginary

part of the refractive index, $\kappa(\omega)$. The real part of the refractive index, $n(\omega)$, is obtained from the phase difference between two signals as

$$n(\omega) = 1 + \frac{\varphi_r - \varphi_s}{2\pi d}\lambda, \quad (25)$$

and the absorption coefficient,

$$\alpha(\omega) = -\frac{2}{d}\ln(T) = -\frac{2}{d}\ln\left(\left(\frac{E_s(\omega)}{E_r(\omega)}\right)^2\right) = \frac{4\pi k}{\lambda}, \quad (26)$$

where φ_r is the phase of the reference waveform, φ_s is the phase of the signal that passed through the sample, and λ is the wavelength. So, in conclusion, the extracted optical parameters from the time-domain THz signals can be used in identifying the substances. On the other hand, the optical characteristics including absorption and refractive index should be further modified in the nanogap antenna system.

To closely investigate how the enhanced electric field can contribute to the detection situation, FDTD numerical simulation was implemented. We adapted a nonuniform meshing tool with a 10-nm gird at minimum to describe

a deep subwavelength thickness of the film. The detectable target samples were assumed as homogeneously dielectric and somewhat absorptive clads with a certain thickness (much less than the wavelength), having the complex refractive index as $A \cdot n + iB \cdot \kappa$, where A and B are constant values over the broadband frequency regime in the range of 1.0–3.0. Using the auxiliary differential equation method, the absorptive media were implanted in the gold nanogap antenna.

Because the directly transmitted THz field passes the absorptive medium with a trend of exponential decay, the reduction of the transmission can be described as $\frac{T_s(\omega)}{T_r(\omega)} = C \cdot e^{-\kappa k(\omega)h}$, where $T_r(\omega) = (E_r(\omega))^2$ and $T_s(\omega) = (E_s(\omega))^2$ are the transmittances through the nanoantenna without and with the clads, C is the transmittance ratio at the air to clad interface, $k = 2\pi/\lambda$ is the incidence momentum, and h is the thickness of the clad, proportional to the molecular concentration (Figure 24A). As the clad increases from 0.5 to 5.0 μm, the transmittance decreases at the resonance frequency, an indication of increased absorption (Figure 24B).

On the one hand, the transmittance can be affected by the complex refractive indices as plotted in Figure 25A. While absorption is accompanied by the change in the imaginary part of the refractive index, κ, the change in the real part of the refractive index, the resonance frequency is mainly affected by n. The various changes in transmission spectra, therefore, can be clear evidence to discriminate the species of the target sensing materials. As plotted in Figure 25B, the peak of transmittance clearly decreases in terms of the imaginary part of the refractive index, κ; meanwhile, the resonance frequency mainly related to the real part of the refractive index, n, shows a small change. However, it should be noted that
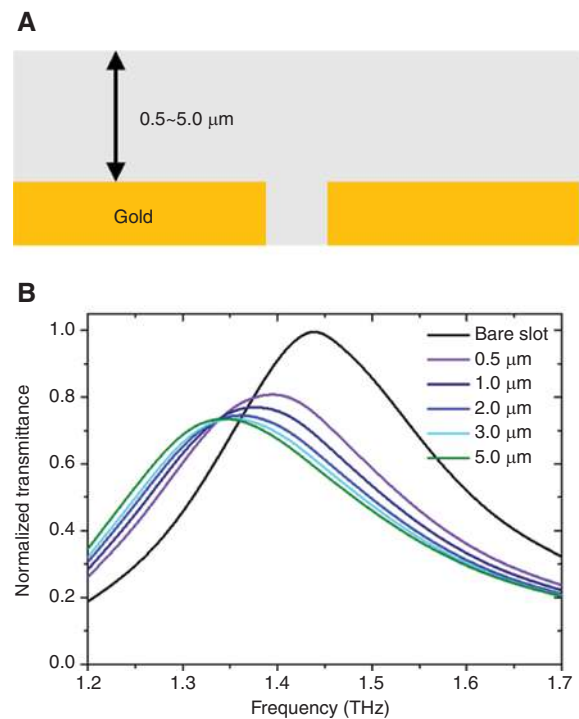
Figure 24: An interpretation of molecule interaction with nano antennas.
(A) Schematic of the cross-section view of the absorptive clad covered onto the gold nanogap antenna. (B) Normalized transmittance to the incidence was calculated for different thickness of clads from 0.5 to 5.0 μm in thickness.

a stronger absorption can give an appreciable change in the resonance frequency.

In Ref. [276], different types of saccharide molecules possessing different molecular vibration modes (e.g. glucose at 1.4 THz and sucrose and fructose at 1.7 THz) were clearly distinguished using different length of gap antenna based sensing chips with different fundamental
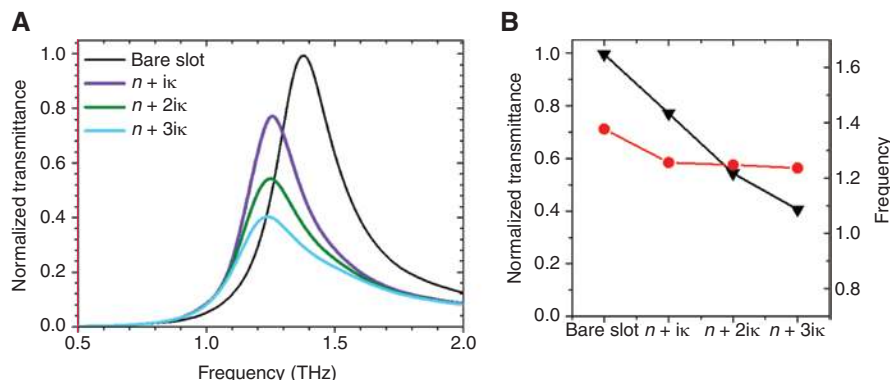
Figure 25: Light transmission with varying imaginary part of the refractive index of the clad.
(A) Normalized transmittance to the incidence was simulated for various complex refractive indices. (B) The peak of the transmittance value and the resonance frequency were plotted in terms of the refractive index.
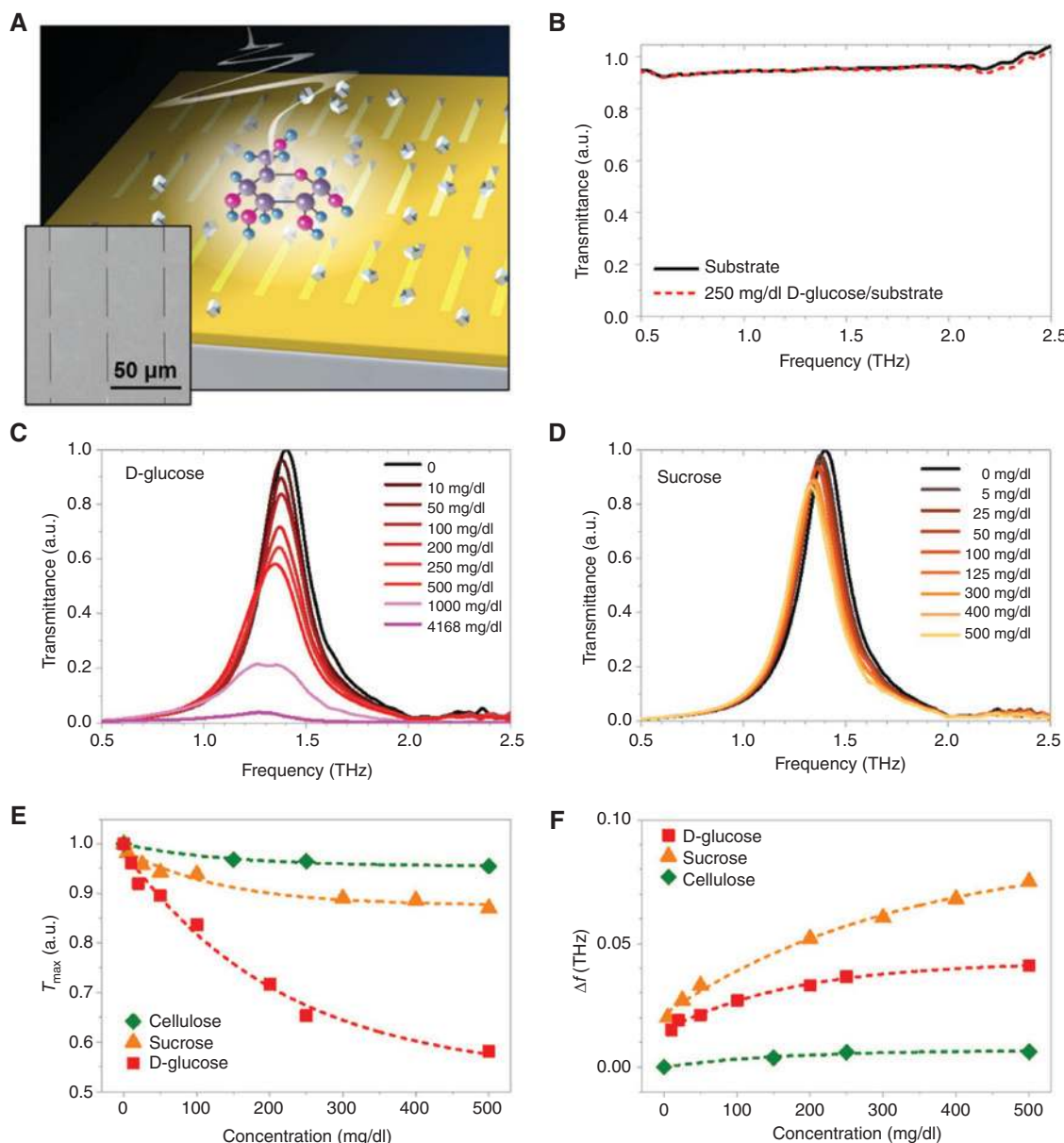
Figure 26: Detection of the sugar molecule by a THz metamaterial.
(A) Schematic of the sugar molecule detection using a nano-antenna array-based sensing chip. (B) Normalized THz spectra measured for a bare substrate used as a substrate and 250 mg/dl of glucose on the same Si substrate. (C) Normalized THz spectra measured with the glucose antenna for D-glucose and (D) sucrose molecules. (E) The changes in the maximum values of the normalized transmittances are plotted for D-glucose, sucrose, and cellulose as a function of the molecular concentration level. (F) Frequency shifts at the maximum transmittance for three samples are plotted. This figure is reproduced from Ref. [276].

resonance frequency as shown in Figure 26. Using glucose-antenna (f_{res} = 1.4 THz), only the glucose sample shows the sensitively changed transmission spectrum; meanwhile, other saccharide samples do not. In the imaging data performed with the fructose-antenna (f_{res} = 1.7 THz), a strongly changed image contrast was observed at the fructose sample dropped area.

Applying this concept to various biomolecules and chemical molecules with specific vibration modes at broadband THz frequency regime, target samples in unprecedentedly low concentration level can be detected. This is valid even in case of more complex biological systems including protein, cell, and tissues with no specific spectral features due to their superposition and broadening of the spectrum. Such relatively large biomaterials can be considered a combination of many proteins, with vibration modes with inhomogeneous broadening such that no recognizable absorption features exist in the
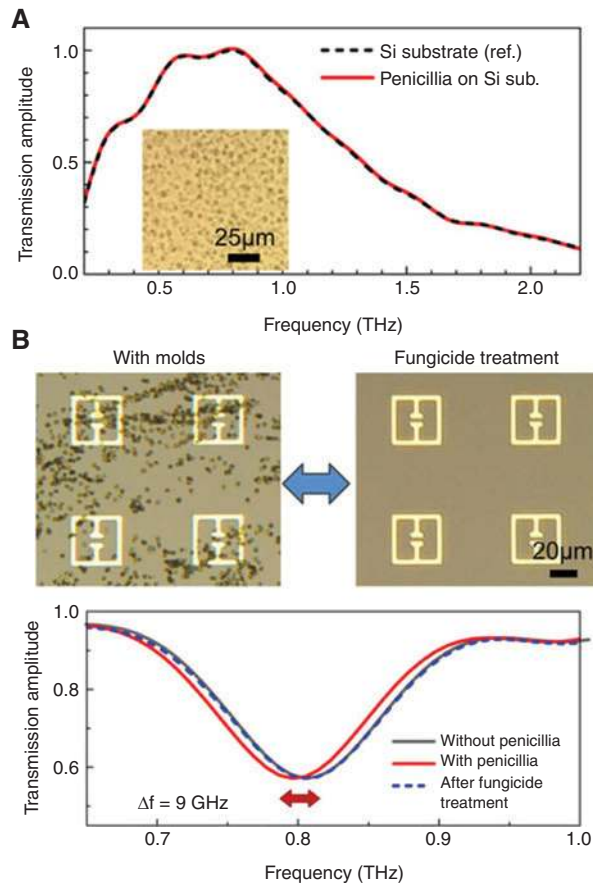
Figure 27: Detection of complex biological system by using THz metamaterial.
(A) THz transmission amplitudes for bare substrate with (red solid line) and without (black dashed line) deposition of penicillia. (B) Microscope images of metamaterials with the deposition of penicillia a (left) and after fungicide treatments (right). (C) THz transmission amplitudes measured before and after the fungicide treatment. This figure is reproduced from Ref. [275].

THz spectrum [292]. In those cases, especially, the spectral shift can be treated as a key parameter. As shown in Figure 27, the resonance frequency shift of the metamaterial by the fungicide treatments is interpreted in terms of the number density and the dielectric constants of the microorganisms inside a gap area.

Besides single resonance gap structures, ultrabroadband resonance filters composed of several gap antennas with log-periodically varied lengths and periods in their arrangement at the same time can be an excellent alternative, utilizing their field-enhancement advantage but freely applicable to any target frequency [57, 189]. Such ultra-broadband sensing chip has a decided merit for unknown targets, in other word, samples without any obvious spectral features in THz fingerprinting. This is very useful to identify and quantify such virus samples as shown in Figure 28 [282].

THz optical characteristics based on the transmission reduction and resonance frequency shift by the covered virus samples can be mapped for different subtypes of the viruses and their quantifications. The suggested sensitive and selective THz detection in the reference provides abundant optical information of measured viruses, suggesting quick and accurate monitoring and rapid diagnosis of viruses.

5 Discussions and outlook

Maxwell's theory provided descriptions of light interaction with metal in terms of microscopic coupling between incident electromagnetic waves and charges residing in metal. This immediately allowed manipulation of the moving of charges by the external light, which is now developed to colossal field enhancement by accumulating charges near a narrow gap in metal. This huge field enhancement is in particular important in the THz spectral regime as it can partly compensate the relatively low average power of THz sources and small cross-sections [293]. Nonlinear THz response [294–299] is a prime example utilizing intense THz field that boosts light-matter interaction [300, 301]. Furthermore, it is very clear that integration of the huge field enhancement in a gap with other novel optical/electrical/plasmonic properties of materials [302–304] or devices [9, 305–313] can expand the practical use of the THz field. Graphene-integrated plasmonic system [34, 129, 314–318] is one immediate example, enabled by atomically thin and electrically tunable nature of graphene (Figure 29). We also expect that, considering the reciprocity of electromagnetic radiation [319], the light-capturing ability of nanogap could be a key principle to extract and radiate THz waves from the integrated devices.

Although we have mainly discussed resonant and nonresonant field enhancements in fundamental types of gaps, i.e. slit and rectangle slot, there are many other opportunities to realize even higher field enhancement. For instance, coupling of two or more symmetric/asymmetric gaps can be considered to obtain field enhancement by symmetric and antisymmetric resonance modes [71, 320, 321]. Also, localizations of incident/transmitted light before/after the gap can be incorporated to increase the field enhancement in the gap [322–325] (Figure 30). The other example is to make use of hybridization of a gap with plasmonic metastructures or metaelements [71, 114, 191, 320–329] that results in intensive localization of electric field in the form of surface waves such as vortex-plasmon and spoof surface plasmon modes.
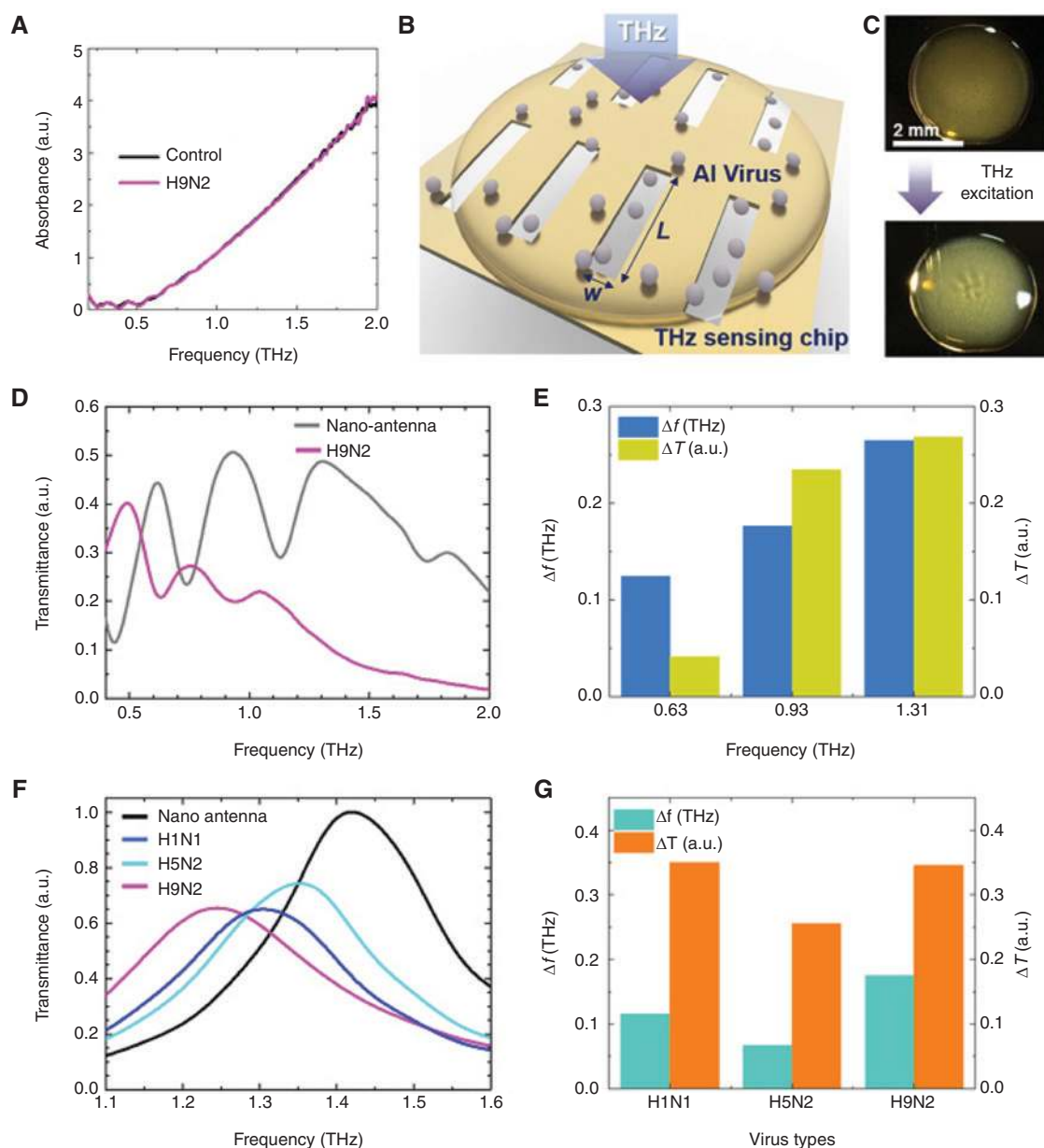
Figure 28: THz metamaterials for versatile detection of molecules.
(A) Absorption spectra for pallet types of virus included a protein sample (H9N2) and a control without virus. (B) THz detection of virus samples in liquid state using a nano slot-antenna array-based sensing chip. (C) Optical images of dropped virus solutions onto the multiresonance nano-antenna array before (top) and after (down) THz excitation. (D) Transmittance spectra through multiresonance nano-antenna with and without H9N2 virus. (E) The difference in transmitted intensity (ΔT) and shifted resonance frequency from each fundamental resonance peak (Δf) for H9N2 virus. This figure is reproduced from Ref. [282].

6 Conclusions

In this review, we discussed both the fundamentals and applications of THz wave interaction with deep subwavelength nanostructures. The enormous THz field enhancement can be explained as a result of surface charge accumulation near the nanogaps, with narrower gaps supporting stronger electric field enhancement. The fundamentals of giant THz field enhancement at an infinitely long nanogap were introduced in Section 2. Specifically, nonresonant THz field enhancements by nanogaps with both sub- and super-skin-depth thicknesses were discussed with a simple model based on the boundary conditions of Maxwell's equations. From this model, we obtained a surprisingly simple description of the field enhancement valid over many orders of magnitudes
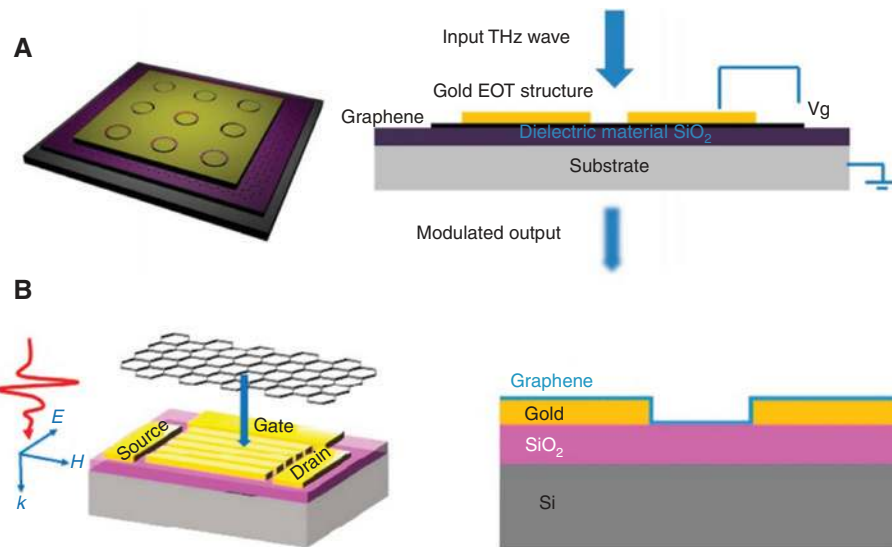
Figure 29: Graphene-integrated plasmonic metal structures for THz modulation, utilizing tunability of graphene and strong local field enhancement.
A hybrid structures of (A) graphene and ring apertures, and (B) graphene and an array of slits. A and B are reproduced from Refs. [34] and [129], respectively.
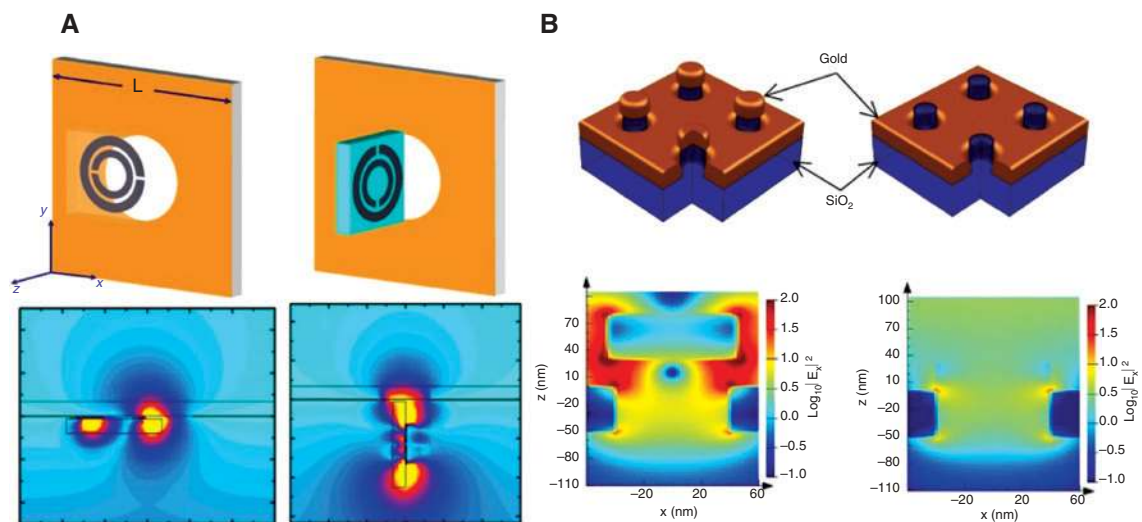
Figure 30: Boosted field enhancements by localization of incident/transmitted light by using additional plasmonic couplers.
(A) Coupling with split-ring-resonators, and (B) plasmonic islands. A and B are reproduced from Refs. [322] and [323], respectively.

of conductivity of metal as well as many orders of magnitudes of the film thickness. In terms of the real-world measurement, we revisited the Kirchhoff integral formalism that enables quantitative estimation of near-field enhancement by typical far-field measurements. At the end of Section 2, resonant THz field enhancement by critically defined boundaries such as rectangular slot shapes was also discussed. In Section 3, more extreme cases with deep subwavelength structures from nanoscale to Angstrom scale were discussed with some example of

plasmonic quantum effect and electron tunneling with consequent nonlinear behaviors. Enhanced THz nonlinear phenomena through nano- to Angstrom-sized gaps show a new pathway for the observation of unprecedented resonant and nonresonant changes in various. In Section 4, finally, a new type of THz molecule sensor based on the field enhancement via subwavelength structures, a promising sensing tool for chemistry, biology, and medical applications was introduced. As one of representative applications, ultrasensitive and highly selective

THz molecule sensor has been suggested. The ultrasensitive THz molecule sensing mechanism follows the huge THz electric field enhancement via nanogap structures, leaving the magnetic field magnitudes almost intact but with very small spatial curvatures introduced, resulting in greatly increased absorption cross-section of the covered substances. Since many intramolecular and intermolecular vibration modes of molecules exist in the THz range, frequency controllable THz metamaterials can be used as special molecule targeted sensors. As a further step, it can be applied for real-time capturing of some of the physical dynamics prominent in biological systems.

References

[1] Nathan CL, Prashant N, Kevin MM, David JN, Sang-Hyun O. Engineering metallic nanostructures for plasmonics and nanophotonics. Rep Prog Phys 2012;75:036501.

[2] Hoffmann MC, Monozon BS, Livshits D, Rafailov EU, Turchinovich D. Terahertz electro-absorption effect enabling femtosecond all-optical switching in semiconductor quantum dots. Appl Phys Lett 2010;97:231108.

[3] Tanoto H, Teng JH, Wu QY, et al. Greatly enhanced continuous-wave terahertz emission by nano-electrodes in a photoconductive photomixer. Nat Photon 2012;6:121–6.

[4] Ju L, Geng B, Horng J, et al. Graphene plasmonics for tunable terahertz metamaterials. Nat Nano 2011;6:630–4.

[5] Shur M. Plasma wave terahertz electronics. Electron Lett 2010;46:S18–21.

[6] Upadhyaya P, Pramanik S, Bandyopadhyay S. Optical transitions in a quantum wire with spin-orbit interaction and its applications in terahertz electronics: Beyond zeroth-order theory. Phys Rev B 2008;77:155439.

[7] Bahramipanah M, Abrishamian MS, Mirtaheri SA, Liu J-M. Ultracompact plasmonic loop–stub notch filter and sensor. Sens Actuator B Chem 2014;194:311–8.

[8] Mittleman DM. Frontiers in terahertz sources and plasmonics. Nat Photon 2013;7:666–9.

[9] Williams CR, Andrews SR, Maier SA, Fernandez-Dominguez AI, Martin Moreno L, Garcia-Vidal FJ. Highly confined guiding of terahertz surface plasmon polaritons on structured metal surfaces. Nat Photon 2008;2:175–9.

[10] Fitzgerald AJ, Berry E, Zinovev NN, Walker GC, Smith MA, Chamberlain JM. An introduction to medical imaging with coherent terahertz frequency radiation. Phys Med Biol 2002;47:R67.

[11] Parrott EPJ, Sun Y, Pickwell-MacPherson E. Terahertz spectroscopy: its future role in medical diagnoses. J Mol Struct 2011;1006:66–76.

[12] Handley JW, Fitzgerald AJ, Berry E, Boyle RD. Wavelet compression in medical terahertz pulsed imaging. Phys Med Biol 2002;47:3885–92.

[13] Zimdars D, Valdmanis JA, White JS, et al. Technology and applications of terahertz imaging non-destructive examination: inspection of space shuttle sprayed on foam insulation. AIP Conf Proc 2005;760:570–7.

[14] Li J, Pi YM. Target detection for terahertz radar networks based on micro-Doppler signatures. Int J Sens Netw 2015;17:115–21.

[15] Semashkin EN, Artyushkina TV. Operating range and all-weather capability of terahertz (0.1 THz) and gigahertz (3–33.3 GHz) radars on horizontal and oblique tracks. J Opt Technol 2015;82:430–5.

[16] Zimdars D, White JS, Stuk G, Chernovsky A, Fichter G, Williamson S. Security and non destructive evaluation application of high speed time domain terahertz imaging. In: 2006 Conference on Lasers and Electro-Optics and 2006 Quantum Electronics and Laser Science Conference, IEEE, May 21–26, 2006, pp. 1–2.

[17] Han SP, Kim N, Lee WH, et al. Real-time imaging of moving living objects using a compact terahertz scanner. Appl Phys Express 2016;9:022501.

[18] Yasui T, Sawanaka KI, Ihara A, Abraham E, Hashimoto M, Araki T. Real-time terahertz color scanner for moving objects. Opt Express 2008;16:1208–21.

[19] Xu KK, Zhang ZY, Yu Q, Wen ZY. J Disp Technol 2016;12:115–21.

[20] Fukunaga K, Hosako I. Innovative non-invasive analysis techniques for cultural heritage using terahertz technology-Techniques innovantes d'analyse non invasive du patrimoine culturel basées sur les technologies térahertz. C R Phys 2010;11:519–26.

[21] Fukunaga K, Hosako I, Kohdzuma Y, et al. Terahertz analysis of an East Asian historical mural painting. J Eur Opt Soc Rapid Publ 2010;5:10024.

[22] Manceau JM, Nevin A, Fotakis C, Tzortzakis S. Terahertz time domain spectroscopy for the analysis of cultural heritage related materials. Appl Phys B 2008;90:365–8.

[23] Lee JW, Seo MA, Park DJ, et al. Shape resonance omni-directional terahertz filters with near-unity transmittance. Opt Express 2006;14:1253–9.

[24] Libon IH, Baumgärtner S, Hempel M, et al. An optically controllable terahertz filter. Appl Phys Lett 2000;76:2821–3.

[25] Mendis R, Nag A, Chen F, Mittleman DM. A tunable universal terahertz filter using artificial dielectrics based on parallel-plate waveguides. Appl Phys Lett 2010;97:131106.

[26] Kaliteevski MA, Brand S, Garvie-Cook J, Abram RA, Chamberlain JM. Terahertz filter based on refractive properties of metallic photonic crystal. Opt Express 2008;16:7330–5.

[27] Lin WH, Wu CJ, Yang TJ, Chang SJ. Terahertz multichanneled filter in a superconducting photonic crystal. Opt Express 2010;18:27155–66.

[28] Lan F, Yang Z, Qi L, Gao X, Shi Z. Terahertz dual-resonance bandpass filter using bilayer reformative complementary metamaterial structures. Opt Lett 2014;39:1709–12.

[29] Heshmat B, Pahlevaninezhad H, Pang Y, et al. Nanoplasmonic terahertz photoconductive switch on GaAs. Nano Lett 2012;12:6255–9.

[30] Rahm M, Li J-S, Padilla WJ. THz wave modulators: a brief review on different modulation techniques. J Infrared Millim Terahertz Waves 2013;34:1–27.

[31] Choi SB, Kyoung JS, Kim HS, et al. Nanopattern enabled terahertz all-optical switching on vanadium dioxide thin film. Appl Phys Lett 2011;98:071105.

[32] Unlu M, Jarrahi M. Miniature multi-contact MEMS switch for broadband terahertz modulation. Opt Express 2014;22:32245–60.

[33] Li J, He J, Hong Z. Terahertz wave switch based on silicon photonic crystals. Appl Opt 2007;46:5034–7.

[34] Gao WL, Shu J, Reichel K, et al. High-contrast terahertz wave modulation by gated graphene enhanced by extraordinary transmission through ring apertures. Nano Lett 2014;14:1242–8.

[35] Liu G, He M, Tian Z, Li J, Liu J. Terahertz surface plasmon sensor for distinguishing gasolines. Appl Opt 2013;52:5695–700.

[36] Astley V, Reichel K, Mendis R, Mittleman DM. Terahertz microfluidic sensing using a parallel-plate waveguide sensor. J Vis Exp 2012;30:e4304.

[37] Alves F, Grbovic D, Kearney B, Karunasiri G. Microelectromechanical systems bimaterial terahertz sensor with integrated metamaterial absorber. Opt Lett 2012;37:1886–8.

[38] Hassani A, Skorobogatiy M. Surface plasmon resonance-like integrated sensor at terahertz frequencies for gaseous analytes. Opt Express 2008;16:20206–14.

[39] Miyamaru F, Hayashi S, Otani C, et al. Terahertz surface-wave resonant sensor with a metal hole array. Opt Lett 2006;31:1118–20.

[40] Xu KK. Integrated silicon directly modulated light source using p-well in standard CMOS technology. IEEE Sens J 2016;16:6184–91.

[41] Lee JW, Park TH, Nordlander P, Mittleman DM. Optimum areal coverage for perfect transmission in a periodic metal hole array. Appl Phys Lett 2010;97:261112.

[42] Lee JW, Seo MA, Kang DH, Khim KS, Jeoung SC, Kim DS. Terahertz electromagnetic wave transmission through random arrays of single rectangular holes and slits in thin metallic sheets. Phys Rev Lett 2007;99:137401.

[43] Deng G, Yang J, Yin Z. Broadband terahertz metamaterial absorber based on tantalum nitride. Appl Opt 2017;56:2449–54.

[44] Gong C, Zhan M, Yang J, et al. Broadband terahertz metamaterial absorber based on sectional asymmetric structures. Sci Rep 2016;6:32466.

[45] Chowdhury DR, Singh R, Reiten M, et al. A broadband planar terahertz metamaterial with nested structure. Opt Express 2011;19:15817–23.

[46] Grant J, Ma Y, Saha S, Khalid A, Cumming DR. Polarization insensitive, broadband terahertz metamaterial absorber. Opt Lett 2011;36:3476–8.

[47] Lee JW, Seo MA, Sohn JY, et al. Invisible plasmonic meta-materials through impedance matching to vacuum. Opt Express 2005;13:10681–7.

[48] Garcia-Vidal FJ, Moreno E, Porto JA, Martin-Moreno L. Transmission of light through a single rectangular hole. Phys Rev Lett 2005;95:103901.

[49] Lee JW, Seo MA, Kim DS, Kang JH, Park Q-H. Polarization dependent transmission through asymmetric C-shaped holes. Appl Phys Lett 2009;94:081102.

[50] Park DJ, Hong JT, Park JK, et al. Resonant transmission of terahertz waves through metallic slot antennas on various dielectric substrates. Curr Appl Phys 2013;13:753–7.

[51] Seo MA, Lee JW, Kim DS. Dielectric constant engineering with polymethylmethacrylate-graphite metastate composites in the terahertz region. J Appl Phys 2006;99:066103.

[52] Kyoung J, Seo M, Park H, et al. Giant nonlinear response of terahertz nanoresonators on VO_2 thin film. Opt Express 2010;18:16452–9.

[53] Berrier A, Ulbricht R, Bonn M, Rivas JG. Ultrafast active control of localized surface plasmon resonances in silicon bowtie antennas. Opt Express 2010;18:23226–35.

[54] Chen HT, O'Hara JF, Azad AK, et al. Experimental demonstration of frequency-agile terahertz metamaterials. Nat Photonics 2008;2:295–8.

[55] Stefanovich G, Pergament A, Stefanovich D. Electrical switching and Mott transition in VO_2. J Phys: Condensed Matter 2000;12:8837.

[56] Jeong YG, Bernien H, Kyoung JS, et al. Electrical control of terahertz nano antennas on VO_2 thin film. Opt Express 2011;19:21211–5.

[57] Seo MA, Kyoung JS, Park HR, et al. Active terahertz nano-antennas based on VO_2 phase transition. Nano Lett 2010;10:2064–8.

[58] Jepsen PU, Fischer BM, Thoman A, et al. Metal-insulator phase transition in a VO2 thin film observed with terahertz spectroscopy. Phys Rev B 2006;74:205103.

[59] Kats MA, Blanchard R, Genevet P, et al. Thermal tuning of mid-infrared plasmonic antenna arrays using a phase change material. Opt Lett 2013;38:368–70.

[60] Wang J, Liu S, Guruswamy S, Nahata A. Reconfigurable terahertz metamaterial device with pressure memory. Opt Express 2014;22:4065–74.

[61] Madugani R, Yang Y, Ward JM, et al. Terahertz tuning of whispering gallery modes in a PDMS stand-alone, stretchable microsphere. Opt Lett 2012;37:4762–4.

[62] Lee S, Kim S, Kim TT, et al. Reversibly stretchable and tunable terahertz metamaterials with wrinkled layouts. Adv Mater 2012;24:3491–7.

[63] Amer N, Hurlbut WC, Norton BJ, Lee YS, Etringer SL, Paul BK. Terahertz wave propagation in one-dimensional periodic dielectrics. Appl Opt 2006;45:1857–60.

[64] Lee JW, Seo MA, Park DJ, et al. Terahertz transparency at Fabry-Perot resonances of periodic slit arrays in a metal plate: experiment and theory. Opt Express 2006;14:12637–43.

[65] Lee J, Seo M, Park D, et al. Shape resonance omni-directional terahertz filters with near-unity transmittance. Opt Express 2006;14:1253–9.

[66] Kang JH, Park QH, Lee JW, Seo MA, Kim DS. Perfect transmission of THz waves in structured metals. J Korean Phys Soc 2006;49:881–4.

[67] Cao H, Nahata A. Resonantly enhanced transmission of terahertz radiation through a periodic array of subwavelength apertures. Opt Express 2004;12:1004–10.

[68] Koo S, Kumar MS, Shin J, Kim D, Park N. Extraordinary magnetic field enhancement with metallic nanowire: role of surface impedance in Babinet's principle for sub-skin-depth regime. Phys Rev Lett 2009;103:263901.

[69] Seo MA, Park HR, Koo SM, et al. Terahertz field enhancement by a metallic nano slit operating beyond the skin-depth limit. Nat Photonics 2009;3:152–6.

[70] Tanoto H, Teng JH, Wu QY, et al. Nano-antenna in a photo-conductive photomixer for highly efficient continuous wave terahertz emission. Sci Rep 2013;3:2824.

[71] Bahk YM, Choi JW, Kyoung J, Park HR, Ahn KJ, Kim DS. Selective enhanced resonances of two asymmetric terahertz nano reso-nators. Opt Express 2012;20:25644–53.

[72] Park HR, Bahk YM, Choe JH, et al. Terahertz pinch harmonics enabled by single nano rods. Opt Express 2011;19:24775–81.

[73] Feuillet-Palma C, Todorov Y, Vasanelli A, Sirtori C. Strong near field enhancement in THz nano-antenna arrays. Sci Rep 2013;3:1361.

[74] Park HR, Bahk YM, Ahn KJ, et al. Controlling terahertz radiation with nanoscale metal barriers embedded in nano slot anten-nas. ACS Nano 2011;5:8340–5.

[75] Chen X, Park HR, Pelton M, et al. Atomic layer lithography of wafer-scale nanogap arrays for extreme confinement of electro-magnetic waves. Nat Commun 2013;4:2361.

[76] Bahk Y-M, Han S, Rhie J, et al. Ultimate terahertz field enhance-ment of single nanoslits. Phys Rev B 2017;95:075424.

[77] Sarychev AK, Shvets G, Shalaev VM. Magnetic plasmon reso-nance. Phys Rev E Stat Nonlin Soft Matter Phys 2006;73(3 Pt 2):036609.

[78] Berry CW, Wang N, Hashemi MR, Unlu M, Jarrahi M. Significant performance enhancement in photoconductive terahertz opto-electronics by incorporating plasmonic contact electrodes. Nat Comm 2013;4:1622.

[79] Kim JY, Kang BJ, Bahk YM, et al. Tunnelling current-voltage characteristics of Angstrom gaps measured with terahertz time-domain spectroscopy. Sci Rep 2016;6:29103.

[80] Bahk YM, Kang BJ, Kim YS, et al. Electromagnetic saturation of angstrom-sized quantum barriers at terahertz frequencies. Phys Rev Lett 2015;115:125501.

[81] Seo M, Kang J-H, Kim H-S, et al. Observation of terahertz-radiation-induced ionization in a single nano island. Sci Rep 2015;5:10280.

[82] Iwaszczuk K, Zalkovskij M, Strikwerda AC, Jepsen PU. Nitrogen plasma formation through terahertz-induced ultrafast electron field emission. Optica 2015;2:116–23.

[83] Jeong Y-G, Paul MJ, Kim S-H, Yee K-J, Kim D-S, Lee Y-S. Large enhancement of nonlinear terahertz absorption in intrinsic GaAs by plasmonic nano antennas. Appl Phys Lett 2013;103:171109.

[84] Lange C, Maag T, Hohenleutner M, et al. Extremely non-perturbative nonlinearities in GaAs driven by atomically strong terahertz fields in gold metamaterials. Phys Rev Lett 2014;113:227401.

[85] Han S, Kim J-Y, Kang T, et al. Colossal terahertz nonlinear-ity in angstrom- and nanometer-sized gaps. ACS Photonics 2016;3:1440–5.

[86] Kim JY, Kang BJ, Park J, et al. Terahertz quantum plasmon-ics of nanoslot antennas in nonlinear regime. Nano Lett 2015;15:6683–8.

[87] Bonod N, Popov E, Gerard D, Wenger J, Rigneault H. Field enhancement in a circular aperture surrounded by a single channel groove. Opt Express 2008;16:2276–87.

[88] Kang JH, Kim DS, Park QH. Local capacitor model for plasmonic electric field enhancement. Phys Rev Lett 2009;102:093906.

[89] Novitsky A, Ivinskaya AM, Zalkovskij M, Malureanu R, Jepsen PU, Lavrinenko AV. Non-resonant terahertz field enhancement in periodically arranged nanoslits. J Appl Phys 2012;112:074318.

[90] Choe JH, Kang JH, Kim DS, Park QH. Slot antenna as a bound charge oscillator. Opt Express 2012;20:6521–6.

[91] García-Vidal FJ, Martín-Moreno L, Moreno E, Kumar LKS, Gordon R. Transmission of light through a single rectangular hole in a real metal. Phys Rev B 2006;74:153411.

[92] Shalaby M, Merbold H, Peccianti M, et al. Concurrent field enhancement and high transmission of THz radiation in nanoslit arrays. Appl Phys Lett 2011;99:041110.

[93] Park SG, Choi Y, Oh YJ, Jeong KH. Terahertz photoconductive antenna with metal nanoislands. Opt Express 2012;20: 25530–5.

[94] Yang Y, Singh R, Zhang W. Anomalous terahertz transmission in bow-tie plasmonic antenna apertures. Opt Lett 2011;36:2901–3.

[95] Maksymov IS, Miroshnichenko AE, Kivshar YS. Actively tun-able bistable optical Yagi-Uda nanoantenna. Opt Express 2012;20:8929–38.

[96] Dorfmuller J, Dregely D, Esslinger M, et al. Near-field dynamics of optical Yagi-Uda nanoantennas. Nano Lett 2011;11:2819–24.

[97] Taminiau TH, Stefani FD, van Hulst NF. Enhanced directional excitation and emission of single emitters by a nano-optical Yagi-Uda antenna. Opt Express 2008;16:10858–6.

[98] Razzari L, Toma A, Shalaby M, et al. Extremely large extinction efficiency and field enhancement in terahertz resonant dipole nanoantennas. Opt Express 2011;19:26088–94.

[99] Razzari L, Toma A, Clerici M, et al. Terahertz dipole nano-antenna arrays: resonance characteristics. Plasmonics 2013;8:133–8.

[100] Gacemi D, Mangeney J, Colombelli R, Degiron A. Subwave-length metallic waveguides as a tool for extreme confinement of THz surface waves. Sci Rep 2013;3:1369.

[101] Toma A, Tuccio S, Prato M, et al. Squeezing terahertz light into nanovolumes: nanoantenna enhanced terahertz spectro-scopy (NETS) of semiconductor quantum dots. Nano Lett 2015;15:386–91.

[102] Jeong J, Rhie J, Jeon W, Hwang CS, Kim DS. High-throughput fabrication of infinitely long 10 nm slit arrays for terahertz applications. J Infrared Millim Terahertz Waves 2015;36:262–8.

[103] Park SJ, Son BH, Choi SJ, Kim HS, Ahn YH. Sensitive detec-tion of yeast using terahertz slot antennas. Opt Express 2014;22:30467–72.

[104] Jeong YG, Paul MJ, Kim SH, Yee KJ, Kim DS, Lee YS. Large enhancement of nonlinear terahertz absorption in intrin-sic GaAs by plasmonic nano antennas. Appl Phys Lett 2013;103:171109.

[105] Shu J, Qiu CY, Astley V, Nickel D, Mittleman DM, Xu QF. High-contrast terahertz modulator based on extraordi-nary transmission through a ring aperture. Opt Express 2011;19:26666–71.

[106] Park HR, Bahk YM, Choe JH, et al. Terahertz pinch harmonics enabled by single nano rods. Opt Express 2011;19:24775–81.

[107] Merbold H, Bitzer A, Feurer T. Second harmonic generation based on strong field enhancement in nanostructured THz materials. Opt Express 2011;19:7262–73.

[108] Dai L, Jiang C. Anomalous near-perfect extraordinary optical absorption on subwavelength thin metal film grating. Opt Express 2009;17:20502–14.

[109] Werley CA, Fan KB, Strikwerda AC, et al. Time-resolved imaging of near-fields in THz antennas and direct quantitative measurement of field enhancements. Opt Express 2012;20:8551–67.

[110] Ogut B, Vogelgesang R, Sigle W, Talebi N, Koch CT, van Aken PA. Hybridized metal slit eigenmodes as an illustration of Babinet's Principle. Acs Nano 2011;5:6701–6.

[111] Yang J, Cao Q, Zhou CH. Theory for terahertz plasmons of metallic nanowires with sub-skin-depth diameters. Opt Express 2010;18:18550–7.

[112] Hu D, Wang XK, Feng SF, et al. Ultrathin terahertz planar elements. Adv Opt Mater 2013;1:186–91.

[113] Iwaszczuk K, Andryieuski A, Lavrinenko A, Zhang XC, Jepsen PU. Terahertz field enhancement to the MV/cm regime in a tapered parallel plate waveguide. Opt Express 2012;20: 8344–55.

[114] Bulgarevich DS, Watanabe M, Shiwa M. Single sub-wavelength aperture with greatly enhanced transmission. New J Phys 2012;14:053001.

[115] Gadalla MN, Abdel-Rahman M, Shamim A. Design, optimization and fabrication of a 28.3 THz nano-rectenna for infrared detection and rectification. Sci Rep 2014;4:4270.

[116] Fan F, Xu ST, Wang XH, Chang SJ. Terahertz polarization converter and one-way transmission based on double-layer magneto-plasmonics of magnetized InSb. Opt Express 2016;24:26431–43.

[117] Low T, Avouris P. Graphene plasmonics for terahertz to mid-infrared applications. Acs Nano 2014;8:1086–101.

[118] Fan F, Gu WH, Chen S, Wang XH, Chang SJ. State conversion based on terahertz plasmonics with vanadium dioxide coating controlled by optical pumping. Opt Lett 2013;38:1582–4.

[119] Panaretos AH, Werner DH. Spoof plasmon radiation using sinusoidally modulated corrugated reactance surfaces. Opt Express 2016;24:2443–56.

[120] Yu N, Wang QJ, Kats MA, et al. Designer spoof surface plasmon structures collimate terahertz laser beams. Nat Mater 2010;9:730–5.

[121] Ishikawa A, Zhang S, Genov DA, Bartal G, Zhang X. Deep subwavelength terahertz waveguides using gap magnetic plasmon. Phys Rev Lett 2009;102:043904.

[122] Chern R-L. Magnetic and surface plasmon resonances for periodic lattices of plasmonic split-ring resonators. Phys Rev B 2008;78:085116.

[123] Martin-Cano D, Quevedo-Teruel O, Moreno E, Martin-Moreno L, Garcia-Vidal FJ. Waveguided spoof surface plasmons with deep-subwavelength lateral confinement. Opt Lett 2011;36:4635–7.

[124] Lee SH, Choi J, Kim HD, Choi H, Min B. Ultrafast refractive index control of a terahertz graphene metamaterial. Sci Rep 2013;3:2135.

[125] Choi M, Lee SH, Kim Y, et al. A terahertz metamaterial with unnaturally high refractive index. Nature 2011;470:369–73.

[126] Chen HT, Padilla WJ, Zide JM, Gossard AC, Taylor AJ, Averitt RD. Active terahertz metamaterial devices. Nature 2006;444: 597–600.

[127] Moser HO, Casse BD, Wilhelmi O, Saw BT. Terahertz response of a microfabricated rod–split-ring-resonator electromagnetic metamaterial. Phys Rev Lett 2005;94:063901.

[128] Wang D, Gu Y, Gong Y, Qiu CW, Hong M. An ultrathin terahertz quarter-wave plate using planar babinet-inverted metasurface. Opt Express 2015;23:11114–22.

[129] Shi SF, Zeng B, Han HL, et al. Optimizing broadband terahertz modulation with hybrid graphene/metasurface structures. Nano Lett 2015;15:372–7.

[130] Takano K, Shibuya K, Akiyama K, Nagashima T, Miyamaru F, Hangyo M. A metal-to-insulator transition in cut-wire-grid metamaterials in the terahertz region. J Appl Phys 2010;107:024907.

[131] Sommerfeld A. Mathematische Theorie der Diffraction. Math Ann 1896;47:317–74.

[132] Sheppard CJ, Lin J, Kou SS. Rayleigh–Sommerfeld diffraction formula in k space. J Opt Soc Am A Opt Image Sci Vis 2013;30:1180–3.

[133] Marathay AS, McCalmont JE. On the usual approximation used in the Rayleigh–Sommerfeld diffraction theory. J Opt Soc Am A Opt Image Sci Vis 2004;21:510–6.

[134] Bouwkamp CJ, Casimir HBG. On multipole expansions in the theory of electromagnetic radiation. Physica 1954;20:539–54.

[135] Bouwkamp CJ. Diffraction theory. Rep Prog Phys 1954;17: 35–100.

[136] Bethe HA. Theory of diffraction by small holes. Phys Rev 1944;66:163–82.

[137] Bouwkamp CJ. On the diffraction of electromagnetic waves by small circular disks and holes. Philips Res Rep 1950;5: 401–22.

[138] Ulrich R. Far-infrared properties of metallic mesh and its complementary structure. Infrared Phys 1967;7:37–55.

[139] Ebbesen TW, Lezec HJ, Ghaemi HF, Thio T, Wolff PA. Extraordinary optical transmission through sub-wavelength hole arrays. Nature 1998;391:667–9.

[140] Kim TJ, Thio T, Ebbesen TW, Grupp DE, Lezec HJ. Control of optical transmission through metals perforated with subwavelength hole arrays. Opt Lett 1999;24:256–8.

[141] Kim DS, Hohng SC, Malyarchuk V, et al. Microscopic origin of surface-plasmon radiation in plasmonic band-gap nanostructures. Phys Rev Lett 2003;91:143901.

[142] Minhas BK, Fan W, Agi K, Brueck SRJ, Malloy KJ. Metallic inductive and capacitive grids: theory and experiment. J Opt Soc Am A 2002;19:1352–9.

[143] Rivas JG, Schotsch C, Bolivar PH, Kurz H. Enhanced transmission of THz radiation through subwavelength holes. Phys Rev B 2003;68:201306.

[144] Naweed A, Baumann F, Bailey WA, Karakashian AS, Goodhue WD. Evidence for radiative damping in surface-plasmon-mediated light transmission through perforated conducting films. J Opt Soc Am B 2003;20:2534–8.

[145] Qu DX, Grischkowsky D. Observation of a new type of THz resonance of surface plasmons propagating on metal-film hole arrays. Phys Rev Lett 2004;93:196804.

[146] Qu DX, Grischkowsky D, Zhang WL. Terahertz transmission properties of thin, subwavelength metallic hole arrays. Opt Lett 2004;29:896–8.

[147] Kang JH, Choe JH, Kim DS, Park QH. Substrate effect on aperture resonances in a thin metal film. Opt Express 2009;17:15652–8.

[148] Gordon R, Brolo A. Increased cut-off wavelength for a sub-wavelength hole in a real metal. Opt Express 2005;13: 1933–8.

[149] Bravo-Abad J, Fernandez-Dominguez AI, Garcia-Vidal FJ, Martin-Moreno L. Theory of extraordinary transmission of light through quasiperiodic arrays of subwavelength holes. Phys Rev Lett 2007;99:203905.

[150] Takakura Y. Optical resonance in a narrow slit in a thick metallic screen. Phys Rev Lett 2001;86:5601–3.

[151] Delgado V, Marques R. Surface impedance model for extraordinary transmission in 1D metallic and dielectric screens. Opt Express 2011;19:25290–7.

[152] Galindo V, Wu CP. Numerical solutions for an infinite phased Ar ray of rectangular waveguides with thick walls. IEEE Trans Antenn Propag 1966;14:149–58.

[153] Sheng P, Stepleman RS, Sanda PN. Exact eigenfunctions for square-wave gratings: Application to diffraction and surface-plasmon calculations. Phys Rev B 1982;26:2907–16.

[154] Garcia-Vidal FJ, Martin-Moreno L, Ebbesen TW, Kuipers L. Light passing through subwavelength apertures. Rev Mod Phys 2010;82:729–87.

[155] Liu H, Lalanne P. Microscopic theory of the extraordinary optical transmission. Nature 2008;452:728–31.

[156] Novitsky A, Zalkovskij M, Malureanu R, Lavrinenko A. Microscopic model of the THz field enhancement in a metal nanoslit. Opt Commun 2011;284:5495–500.

[157] He XY. Numerical analysis of the propagation properties of subwavelength semiconductor slit in the terahertz region. Opt Express 2009;17:15359–71.

[158] Bell PM, Pendry JB, Moreno LM, Ward AJ. A program for calculating photonic band structures and transmission coefficients of complex structures. Comput Phys Commun 1995;85:306–22.

[159] Li LF. New formulation of the Fourier modal method for crossed surface-relief gratings. J Opt Soc Am A 1997;14:2758–67.

[160] Salomon L, Grillot F, Zayats AV, de Fornel F. Near-field distribution of optical transmission of periodic subwavelength holes in a metal film. Phys Rev Lett 2001;86:1110–3.

[161] Baida FI, Van Labeke D. Near-field distribution of optical transmission of periodic subwavelength holes in a metal film. Phys Rev B 2003;67:155314.

[162] Bagiante S, Enderli F, Fabianska J, Sigg H, Feurer T. Giant electric field enhancement in split ring resonators featuring nanometer-sized gaps. Sci Rep 2015;5:8051.

[163] Shalaby M, Hauri CP. Air nonlinear dynamics initiated by ultra-intense lambda-cubic terahertz pulses. Appl Phys Lett 2015;106:181108.

[164] Leitenstorfer A, Nelson KA, Reimann K, Tanaka K. Focus on nonlinear terahertz studies. New J Phys 2014;16:045016.

[165] Kampfrath T, Tanaka K, Nelson KA. Resonant and nonresonant control over matter and light by intense terahertz transients. Nat Photonics 2013;7:680–90.

[166] Hebling J, Yeh K-L, Hoffmann MC, Nelson KA. High-power THz generation, THz nonlinear optics, and THz nonlinear spectroscopy. IEEE J Sel Top Quant 2008;14:345–53.

[167] Choi HJ, Baek IH, Kang BJ, et al. Control of terahertz nonlinear transmission with electrically gated graphene metadevices. Sci Rep 2017;7:42833.

[168] Hwang HY, Fleischer S, Brandt NC, et al. A review of non-linear terahertz spectroscopy with ultrashort tabletop-laser pulses. J Mod Optic 2015;62:1447–9.

[169] Chen F, Goodfellow J, Liu S, et al. Ultrafast terahertz gating of the polarization and giant nonlinear optical response in BiFeO$_3$ thin films. Adv Mater 2015;27:6371–5.

[170] Lin J, Oh SH, Nguyen HM, Reitich F. Volume polarization holographic recording in thick photopolymer for optical memory. Opt Express 2014;22:14402–10.

[171] Yasuda H, Hosako I. Terahertz waveguide design for GaSb/AlGaSb quantum cascade laser. Jpn J Appl Phys 2008;47:1632–4.

[172] Ordal MAB, Bell RJ, Jr., Alexander RW, Long LL, Querry MR. Optical properties of Au, Ni, and Pb at submillimeter wavelengths. Appl Optics 1987;26:744–52.

[173] Ordal MAB, Bell RJ, Jr., Alexander RW, Jr., Long LL, Querry MR. Optical properties of fourteen metals in the infrared and far infrared: Al, Co, Cu, Au, Fe, Pb, Mo, Ni, Pd, Pt, Ag, Ti, V, and W. Appl Optics 1985;24:4493–9.

[174] Azad AKZ, Zhao Y, Zhang W, He M. Effect of dielectric properties of metals on terahertz transmission subwavelength hole arrays. Opt Lett 2006;31:2637–9.

[175] Singh R, Azad AK, O'Hara JF, Taylor AJ, Zhang W. Effect of metal permittivity on resonant properties of terahertz metamaterials. Opt Lett 2008;33:1506–8.

[176] Ordal MAL, Long L, Bell RJ, et al. Optical properties of the metals Al, Co, Cu, Au, Fe, Pb, Ni, Pd, Pt, Ag, Ti, and W in the infrared and far infrared. Appl Optics 1983;22:1099–120.

[177] Kang J-H, Park QH. Local enhancement of terahertz waves in structured metals. IEEE T Thz Sci Techn 2016;6: 371–81.

[178] Adam AJL. Review of near-field terahertz measurement methods and their applications. J Infrared, Millim Terahertz Waves 2011;32:976.

[179] Adam AJL, Brok JM, Seo MA, et al. Advanced terahertz electric near-field measurements at sub-wavelength diameter metallic apertures. Opt Express 2008;16:7407–17.

[180] Ahn KJ, Lee KG, Kihm HW, et al. Optical and terahertz near-field studies of surface plasmons in subwavelength metallic slits. New J Phys 2008;10:105003.

[181] Blanchard F, Doi A, Tanaka T, et al. Real-time terahertz near-field microscope. Opt Express 2011;19:8277–84.

[182] Giannini V, Berrier A, Maier SA, Sánchez-Gil JA, Rivas JG. Scattering efficiency and near field enhancement of active semiconductor plasmonic antennas at terahertz frequencies. Opt Express 2010;18:2797–807.

[183] Knab JR, Adam AJL, Nagel M, et al. Terahertz near-field vectorial imaging of subwavelength apertures and aperture arrays. Opt Express 2009;17:15072–86.

[184] Seo MA, Adam AJL, Kang JH, et al. Near field imaging of terahertz focusing onto rectangular apertures. Opt Express 2008;16:20484–9.

[185] Seo MA, Adam AJL, Kang JH, et al. Fourier-transform terahertz near-field imaging of one-dimensional slit arrays: mapping of electric-field-, magnetic-field-, and Poynting vectors. Opt Express 2007;15:11781–9.

[186] Marchand EW, Wolf E. Boundary diffraction wave in the domain of the Rayleigh–Kirchhoff diffraction theory. J Opt Soc Am 1962;52:761–7.

[187] Spence RD. A note on the Kirchhoff approximation in diffraction theory. J Acoust Soc Am 1949;21:98–100.

[188] Kyoung JS, Seo MA, Park HR, Ahn KJ, Kim DS. Far field detection of terahertz near field enhancement of sub-wavelength slits using Kirchhoff integral formalism. Opt Commun 2010;283:4907–10.

[189] Park HR, Koo SM, Suwal OK, et al. High-performance organic charge trap flash memory devices based on ink-jet printed

6,13-bis(triisopropylsilylethynyl) pentacene transistors. Appl Phys Lett 2010;96:213107.

[190] Park DJ, Choi SB, Ahn YH, et al. Terahertz near-field enhancement in narrow rectangular apertures on metal film. Opt Express 2009;17:12493–501.

[191] Kang JH, Park QH. Fractional tunnelling resonance in plasmonic media. Sci Rep 2013;3:2423.

[192] Lee K, Jeong J, Bahk Y-M, et al. Microwave funneling through Sub-10 nm nanogaps. ACS Photonics 2016;3:537–42.

[193] Suwal OK, Rhie J, Kim N, Kim DS. Nonresonant 10⁴ terahertz field enhancement with 5-nm slits. Sci Rep 2017;7:45638.

[194] Han S, Bahk YM, Park N, Kim DS. Terahertz field enhancement in asymmetric and tapered nano-gaps. Opt Express 2016;24:2065–71.

[195] Lu X, Wan R, Wang G, Zhang T, Zhang W. Giant and tunable electric field enhancement in the terahertz regime. Opt Express 2014;22:27001–6.

[196] Ahn JS, Kang T, Singh DK, et al. Optical field enhancement of nanometer-sized gaps at near-infrared frequencies. Opt Express 2015;23:4897–907.

[197] Lu W. Tunable broadband optical field enhancement in graphene-based slot waveguide at infrared frequencies. Appl Opt 2016;55:5095–101.

[198] Garcia-Vidal FJ, Lezec HJ, Ebbesen TW, Martin-Moreno L. Multiple paths to enhance optical transmission through a single subwavelength slit. Phys Rev Lett 2003;90:213901.

[199] Lee KG, Park QH. Coupling of surface plasmon polaritons and light in metallic nanoslits. Phys Rev Lett 2005;95:103902.

[200] Gorelick S, Guzenko VA, Vila-Comamala J, David C. Direct e-beam writing of dense and high aspect ratio nanostructures in thick layers of PMMA for electroplating. Nanotechnology 2010;21:295303.

[201] Tseng AA, Kuan C, Chen CD, Ma KJ. Electron beam lithography in nanoscale fabrication: recent development. IEEE Transactions on Electronics Packaging Manufacturing 2003;26:141–9.

[202] Vieu C, Carcenac F, Pépin A, et al. Electron beam lithography: resolution limits and applications. Appl Surf Sci 2000;164:111–7.

[203] Perry MD, Stuart BC, Banks PS, Feit MD, Yanovsky V, Rubenchik AM. Ultrashort-pulse laser machining of dielectric materials. J Appl Phys 1999;85:6803–10.

[204] Meijer J, Du K, Gillner A, et al. Laser machining by short and ultrashort pulses, state of the art and new opportunities in the age of the photons. CIRP Annals – Manufacturing Technology 2002;51:531–50.

[205] Lee JW, Seo MA, Kim DS, et al. Efficient hole injection in organic light-emitting diodes using C60 as a buffer layer for Al reflective anodes. Appl Phys Lett 2006;88:073512.

[206] Morozov GV, Maev RG, Drake GW. Green's function analysis of electromagnetic waves in two-layered periodic structures with fluctuations in thickness. Phys Rev E Stat Nonlin Soft Matter Phys 2001;63(5 pt 2):056601.

[207] Nicorovici NA, McPhedran RC, Petit R. Efficient calculation of the Green's function for electromagnetic scattering by gratings. Phys Rev E Stat Phys Plasmas Fluids Relat Interdiscip Topics 1994;49:4563–77.

[208] Lalanne P, Hugonin JP. Numerical performance of finite-difference modal methods for the electromagnetic analysis of one-dimensional lamellar gratings. J Opt Soc Am A Opt Image Sci Vis 2000;17:1033–42.

[209] Grober RD, Rutherford T, Harris TD. Modal approximation for the electromagnetic field of a near-field optical probe. Appl Opt 1996;35:3488–95.

[210] Xu KK, Liu SY, Sun WF, et al. Design and fabrication of a monolithic optoelectronic integrated Si CMOS LED based on hot-carrier effect. IEEE J Sel Top Quant 2016;22:2000508.

[211] Tserkezis C, Maack JR, Liu Z, Wubs M, Mortensen NA. Robustness of the far-field response of nonlocal plasmonic ensembles. Sci Rep 2016;6:28441.

[212] Girard C, Cuche A, Dujardin E, Arbouet A, Mlayah A. Molecular decay rate near nonlocal plasmonic particles. Opt Lett 2015;40:2116–9.

[213] Filter R, Bosel C, Toscano G, Lederer F, Rockstuhl C. Nonlocal effects: relevance for the spontaneous emission rates of quantum emitters coupled to plasmonic structures. Opt Lett 2014;39:6118–21.

[214] Varas A, García-González P, Feist J, García-Vidal FJ, Rubio A. Quantum plasmonics: from jellium models to *ab initio* calculations. Nanophotonics 2016;5:409–26.

[215] Qian H, Xiao Y, Lepage D, Chen L, Liu Z. Quantum electrostatic model for optical properties of nanoscale gold films. Nanophotonics 2015;4:413–8.

[216] Raza S, Wubs M, Bozhevolnyi SI, Mortensen NA. Nonlocal study of ultimate plasmon hybridization. Opt Lett 2015;40:839–42.

[217] Teperik TV, Nordlander P, Aizpurua J, Borisov AG. Robust subnanometric plasmon ruler by rescaling of the nonlocal optical response. Phys Rev Lett 2013;110:263901.

[218] Xie HY, Ng MY, Chang YC. Analytical solutions to light scattering by plasmonic nanoparticles with nearly spherical shape and nonlocal effect. J Opt Soc Am A Opt Image Sci Vis 2010;27:2411–22.

[219] Hajisalem G, Min Q, Gelfand R, Gordon R. Effect of surface roughness on self-assembled monolayer plasmonic ruler in nonlocal regime. Opt Express 2014;22:9604–10.

[220] Wiener A, Duan H, Bosman M, et al. Electron-energy loss study of nonlocal effects in connected plasmonic nanoprisms. Acs Nano 2013;7:6287–96.

[221] Podolskiy VA, Ginzburg P, Wells B, Zayats AV. Light emission in nonlocal plasmonic metamaterials. Faraday Discuss 2015;178:61–70.

[222] Toscano G, Raza S, Jauho AP, Mortensen NA, Wubs M. Modified field enhancement and extinction by plasmonic nanowire dimers due to nonlocal response. Opt Express 2012;20:4176–88.

[223] Tserkezis C, Stefanou N, Wubs M, Mortensen NA. Molecular fluorescence enhancement in plasmonic environments: exploring the role of nonlocal effects. Nanoscale 2016;8:17532–41.

[224] Huang Q, Bao F, He S. Nonlocal effects in a hybrid plasmonic waveguide for nanoscale confinement. Opt Express 2013;21:1430–9.

[225] Wiener A, Fernandez-Dominguez AI, Horsfield AP, Pendry JB, Maier SA. Nonlocal effects in the nanofocusing performance of plasmonic tips. Nano Lett 2012;12:3308–14.

[226] Shen H, Chen L, Ferrari L, et al. Optical observation of plasmonic nonlocal effects in a 2D superlattice of ultrasmall gold nanoparticles. Nano Lett 2017;17:2234–9.

[227] Fernandez-Dominguez AI, Wiener A, Garcia-Vidal FJ, Maier SA, Pendry JB. Transformation-optics description of non-

local effects in plasmonic nanostructures. Phys Rev Lett 2012;108:106802.

[228] Mortensen NA, Raza S, Wubs M, Sondergaard T, Bozhevolnyi SI. A generalized non-local optical response theory for plasmonic nanostructures. Nat Commun 2014;5:3809.

[229] McMahon JM, Gray SK, Schatz GC. Optical properties of nanowire dimers with a spatially nonlocal dielectric function. Nano Lett 2010;10:3473–81.

[230] Raza S, Bozhevolnyi SI, Wubs M, Asger Mortensen N. Nonlocal optical response in metallic nanostructures. J Phys Condens Matter 2015;27:183204.

[231] Gao Y, Yuan Z, Gao S. Semiclassical approach to plasmon–electron coupling and Landau damping of surface plasmons. J Chem Phys 2011;134:134702.

[232] Benisti D, Strozzi DJ, Gremillet L, Morice O. Nonlinear Landau damping rate of a driven plasma wave. Phys Rev Lett 2009;103:155002.

[233] Curtet M, Bonnaud G. Landau damping of an electron plasma wave in a plasma with modulated density. Phys Rev E Stat Phys Plasmas Fluids Relat Interdisc Topics 1999;60:R5052–5.

[234] Paredes-Juarez A, Iakushev DA, Flores-Desirena B, Makarov NM, Perez-Rodriguez F. Landau damping of electromagnetic transport via dielectric-metal superlattices. Opt Lett 2015;40:3588–91.

[235] Takida Y, Nawata K, Suzuki S, Asada M, Minamide H. Nonlinear optical detection of terahertz-wave radiation from resonant tunneling diodes. Opt Express 2017;25:5389–96.

[236] Yoshida K, Shibata K, Hirakawa K. Terahertz field enhancement and photon-assisted tunneling in single-molecule transistors. Phys Rev Lett 2015;115:138302.

[237] Ganichev SD, Yassievich IN, Prettl W. Tunneling processes induced by terahertz electric fields. J Biol Phys 2003;29: 327–34.

[238] Kim G, Suh HH, Lee EH. Green's-function study of the electron tunneling in a double-barrier heterostructure. Phys Rev B Condens Matter 1995;52:2632–9.

[239] Li B, Zeng C, Zhao J, Yang J, Hou JG, Zhu Q. Single-electron tunneling spectroscopy of single C_{60} in double-barrier tunnel junction. J Chem Phys 2006;124:64709.

[240] Bomze Y, Gershon G, Shovkun D, Levitov LS, Reznikov M. Measurement of counting statistics of electron transport in a tunnel junction. Phys Rev Lett 2005;95:176601.

[241] Lee JW, Seo MA, Kim DS, et al. Fabry–Perot effects in THz time-domain spectroscopy of plasmonic band-gap structures. Appl Phys Lett 2006;88:071114.

[242] Ward DW, Statz ER, Nelson KA. Fabrication of polaritonic structures in LiNbO3 and LiTaO3 using femtosecond laser machining. Appl Phys A 2007;86:49–54.

[243] Enkrich C, Pérez-Willard F, Gerthsen D, et al. Focused-ion-beam nanofabrication of near-infrared magnetic metamaterials. Adv Mat 2005;17:2547–9.

[244] Ocelic N, Hillenbrand R. Subwavelength-scale tailoring of surface phonon polaritons by focused ion-beam implantation. Nat Mater 2004;3:606–9.

[245] Park H-R, Chen X, Nguyen N-C, Peraire J, Oh S-H. Nanogap-enhanced terahertz sensing of 1 nm Thick (λ/106) dielectric films. ACS Photonics 2015;2:417–24.

[246] Lin C, Chen C, Schneider GJ, et al. Wavelength scale terahertz two-dimensional photonic crystal waveguides. Opt Express 2004;12:5723–8.

[247] Chen H-T, O'Hara JF, Azad AK, et al. Experimental demonstration of frequency-agile terahertz metamaterials. Nat Photon 2008;2:295–8.

[248] Singh R, Plum E, Menzel C, et al. Terahertz metamaterial with asymmetric transmission. Phys Rev B 2009;80:153104.

[249] Lindquist NC, Nagpal P, McPeak KM, Norris DJ, Oh SH. Engineering metallic nanostructures for plasmonics and nanophotonics. Rep Prog Phys 2012;75:036501.

[250] Park W, Rhie J, Kim NY, Hong S, Kim DS. Sub-10 nm feature chromium photomasks for contact lithography patterning of square metal ring arrays. Sci Rep 2016;6:23823.

[251] Beesley DJ, Semple J, Krishnan Jagadamma L, et al. Sub-15-nm patterning of asymmetric metal electrodes and devices by adhesion lithography. Nat Commun 2014;5:3933.

[252] Yoshioka K, Minami Y, Shudo K, et al. Terahertz-field-induced nonlinear electron delocalization in Au nanostructures. Nano Lett 2015;15:1036–40.

[253] Yoshioka K, Katayama I, Minami Y, et al. Real-space coherent manipulation of electrons in a single tunnel junction by single-cycle terahertz electric fields. Nat Photonics 2016;10:762–5.

[254] Simmons JG. Generalized formula for the electric tunnel effect between similar electrodes separated by a thin insulating film. J Appl Phys 1963;34:1793–803.

[255] Fischer BM, Walther M, Jepsen PU. Far-infrared vibrational modes of DNA components studied by terahertz time-domain spectroscopy. Phys Med Biol 2002;47:3807.

[256] King MD, Ouellette W, Korter TM. Noncovalent interactions in paired DNA nucleobases investigated by terahertz spectroscopy and solid-state density functional theory. J Phys Chem A 2011;115:9467–78.

[257] Nishizawa J-I, Sasaki T, Suto K, et al. THz transmittance measurements of nucleobases and related molecules in the 0.4- to 5.8-THz region using a GaP THz wave generator. Opt Commun 2005;246:229–39.

[258] Rungsawang R, Ueno Y, Tomita I, Ajito K. Angle-dependent terahertz time-domain spectroscopy of amino acid single crystals. J Phys Chem B 2006;110:21259–63.

[259] Yamaguchi M, Miyamaru F, Yamamoto K, Tani M, Hangyo M. Terahertz absorption spectra of L, D, and DL-alanine and their application to determination of enantiometric composition. Appl Phys Lett 2005;86:053903.

[260] Korter TM, Balu R, Campbell MB, Beard MC, Gregurick SK, Heilweil EJ. Terahertz spectroscopy of solid serine and cysteine. Chem Phys Lett 2006;418:65–70.

[261] Yamamoto K, Tominaga K, Sasakawa H, et al. Terahertz time-domain spectroscopy of amino acids and poly-peptides. Biophys J 2005;89:L22–4.

[262] Xu J, Plaxco KW, Allen SJ. Probing the collective vibrational dynamics of a protein in liquid water by terahertz absorption spectroscopy. Prot Sci 2006;15:1175–81.

[263] Kim SJ, Born B, Havenith M, Gruebele M. Real-time detection of protein-water dynamics upon protein folding by terahertz absorption spectroscopy. Angewandte Chemie International Edition 2008;47:6486–9.

[264] Markelz AG, Knab JR, Chen JY, He Y. Protein dynamical transition in terahertz dielectric response. Chem Phys Lett 2007;442:413–7.

[265] Woodward RM, Wallace VP, Pye RJ, et al. Terahertz pulse imaging of ex vivo basal cell carcinoma. J Invest Dermatol 2003;120:72–8.

[266] Woodward RM, Wallace VP, Arnone DD, Linfield EH, Pepper M. Terahertz pulsed imaging of skin cancer in the time and frequency domain. J Biol Phys 2003;29:257–9.

[267] Nakajima S, Hoshina H, Yamashita M, Otani C, Miyoshi N. Terahertz imaging diagnostics of cancer tissues with a chemometrics technique. Appl Phys Lett 2007;90:041102.

[268] Oh SJ, Kang J, Maeng I, et al. Nanoparticle-enabled terahertz imaging for cancer diagnosis. Opt Express 2009;17: 3469–75.

[269] Ruth MW, Bryan EC, Vincent PW, et al. Terahertz pulse imaging in reflection geometry of human skin cancer and skin tissue. Phys Med Biol 2002;47:3853.

[270] Löffler T, Bauer T, Siebert KJ, Roskos HG, Fitzgerald A, Czasch S. Terahertz dark-field imaging of biomedical tissue. Opt Express 2001;9:616–21.

[271] Mittleman DM, Jacobsen RH, Nuss MC. T-ray imaging. IEEE J Sel Top Quantum Electronics 1996;2:679–92.

[272] Hu BB, Nuss MC. Imaging with THz waves. Opt Lett 1995;20:1716–8.

[273] Walther M, Fischer B, Schall M, Helm H, Jepsen PU. Far-infrared vibrational spectra of all-*trans*, 9-*cis* and 13-*cis* retinal measured by THz time-domain spectroscopy. Chem Phys Lett 2000;332:389–95.

[274] Park H-R, Ahn KJ, Han S, Bahk Y-M, Park N, Kim D-S. Colossal absorption of molecules inside single terahertz nanoantennas. Nano Lett 2013;13:1782–1786.

[275] Park SJ, Hong JT, Choi SJ, et al. Detection of microorganisms using terahertz metamaterials. Sci Rep 2014;4:4988.

[276] Lee D-K, Kang J-H, Lee J-S, et al. Highly sensitive and selective sugar detection by terahertz nano-antennas. Sci Rep 2015;5:15459.

[277] Zhang C, Liang L, Ding L, et al. Highly sensitive and selective sugar detection by terahertz nano-antennas. Appl Phys Lett 2016;108:241105.

[278] Bui TS, Dao TD, Dang LH, et al. Metamaterial-enhanced vibrational absorption spectroscopy for the detection of protein molecules. Sci Rep 2016;6:32123.

[279] Shih K, Pitchappa P, Manjappa M, Ho CP, Singh R, Lee C. Microfluidic metamaterial sensor: Selective trapping and remote sensing of microparticles. J Appl Phys 2017;121:023102.

[280] Yahiaoui R, Strikwerda AC, Jepsen PU. Terahertz plasmonic structure with enhanced sensing capabilities. IEEE Sensors Journal 2016;16:2484–8.

[281] Hu X, Xu G, Wen L, et al. Metamaterial absorber integrated microfluidic terahertz sensors. Laser Photon Rev 2016;10:962–9.

[282] Lee D-K, Kang J-H, Kwon J, et al. Nano metamaterials for ultra-sensitive Terahertz biosensing. Sci Rep 2017;7:8146.

[283] Xie LJ, Gao WL, Shu J, Ying YB, Kono JC. Extraordinary sensitivity enhancement by metasurfaces in terahertz detection of antibiotics. Sci Rep 2015;5:8671.

[284] Xu KK, Snyman LW, Aharoni H. Si light-emitting device in integrated photonic CMOS ICs. Opt Mater 2017;69:274–82.

[285] Luo L, Ge C, Tao Y, et al. High-eflciency refractive index sensor based on the metallic nanoslit arrays with gain-assisted materials. Nanophotonics 2016;5:139–46.

[286] Ahn KJ, Bahk Y-M, Kim D-S, Kyoung J, Rotermund F. Ultrasensitive molecular absorption detection using metal slot antenna arrays. Opt Express 2015;23:19047–55.

[287] Lee D-K, Kim G, Kim C, et al. Ultrasensitive detection of residual pesticides using THz near-field enhancement. IEEE Trans THz Sci Technol 2016;6:389–95.

[288] Zanchetta G, Lanfranco R, Giavazzi F, Bellini T, Buscaglia M. Emerging applications of label-free optical biosensors. Nanophotonics 2017;6:627–45.

[289] Chiavaioli F, Baldini F, Tombelli S, Trono C, Giannetti A. Biosensing with optical fiber gratings. Nanophotonics 2017;6:663–79.

[290] Upadhya PC, Shen YC, Davies AG, Linfield EH. Terahertz time-domain spectroscopy of glucose and uric acid. J Biol Phys 2003;29:117–21.

[291] Walther M, Fischer BM, Uhd Jepsen P. Noncovalent intermolecular forces in polycrystalline and amorphous saccharides in the far infrared. Chem Phys 2003;288:261–8.

[292] Acbas G, Niessen KA, Snell EH, Markelz AG. Optical measurements of long-range protein vibrations. Nat Commun 2014;5:3076.

[293] Shalaby M, Vicario C, Hauri CP. Demonstration of a low frequency three-dimensional terahertz bullet with extreme brightness. Nat Commun 2015;6:5976.

[294] Kang BJ, Baek IH, Lee SH, et al. Highly nonlinear organic crystal OHQ-T for efficient ultra-broadband terahertz wave generation beyond 10 THz. Opt Express 2016;24: 11054–61.

[295] Gaal P, Reimann K, Woerner M, Elsaesser T, Hey R, Ploog KH. Nonlinear Terahertz Response of *n*-Type GaAs. Phys Rev Lett 2006;96:187402.

[296] Liu RB, Zhu BF. Nonlinear optics of semiconductors under an intense terahertz field. Phys Rev B 2003;68:195206.

[297] Citrin DS. Toward a semiconductor-based terahertz nonlinear medium. Physica E 2001;11:252–6.

[298] Shinokita K, Hirori H, Nagai M, Satoh N, Kadoya Y, Tanaka K. Dynamical Franz–Keldysh effect in GaAs/AlGaAs multiple quantum wells induced by single-cycle terahertz pulses. Appl Phys Lett 2010;97:211902.

[299] Hughes S, Citrin DS. Creation of highly anisotropic wave packets in quantum wells: dynamical Franz-Keldysh effect in the optical and terahertz regimes. Phys Rev B 1999;59:R5288–91.

[300] Liu WW, Wang B, Ke SL, et al. Enhanced plasmonic nanofocusing of terahertz waves in tapered graphene multilayers. Opt Express 2016;24:14765–80.

[301] Jessop DS, Kindness SJ, Xiao L, et al. Graphene based plasmonic terahertz amplitude modulator operating above 100 MHz. Appl Phys Lett 2016;108:171101.

[302] Hong JT, Park DJ, Yim JH, et al. Dielectric constant engineering of single-walled carbon nanotube films for metamaterials and plasmonic devices. J Phys Chem Lett 2013;4:3950–7.

[303] Kang JH, Wang S, Shi ZW, Zhao WY, Yablonovitch E, Wang F. Goos-Hänchen shift and even-odd peak oscillations in edge-reflections of surface polaritons in atomically thin crystals. Nano Lett 2017;17:1768–74.

[304] Chen JN, Badioli M, Alonso-Gonzalez P, et al. Optical nano-imaging of gate-tunable graphene plasmons. Nature 2012;487:77–81.

[305] Novitsky A, Zalkovskij M, Malureanu R, Jepsen PU, Lavrinenko AV. Optical waveguide mode control by nanoslit-enhanced terahertz field. Opt Lett 2012;37:3903–5.

[306] Chevalier P, Bouchon P, Greffet JJ, Pelouard JL, Haidar R, Pardo F. Giant field enhancement in electromagnetic Helmholtz nanoantenna. Phys Rev B 2014;90:195412.

[307] Liu MK, Hwang HY, Tao H, et al. Terahertz-field-induced insulator-to-metal transition in vanadium dioxide metamaterial. Nature 2012;487:345–8.

[308] Grady NK, Heyes JE, Chowdhury DR, et al. Terahertz metamaterials for linear polarization conversion and anomalous refraction. Science 2013;340:1304–7.

[309] Linden S, Enkrich C, Wegener M, Zhou JF, Koschny T, Soukoulis CM. Magnetic response of metamaterials at 100 terahertz. Science 2004;306:1351–3.

[310] Paradiso N, Yaghobian F, Lange C, et al. Tailored nanoantennas for directional Raman studies of individual carbon nanotubes. Phys Rev B 2015;91:235449.

[311] Tao H, Landy NI, Bingham CM, Zhang X, Averitt RD, Padilla WJ. A metamaterial absorber for the terahertz regime: design, fabrication and characterization. Opt Express 2008;16: 7181–8.

[312] Chen HT, Yang H, Singh R, et al. Tuning the resonance in high-temperature superconducting terahertz metamaterials. Phys Rev Lett 2010;105:247402.

[313] Zhao XG, Zhang JD, Fan KB, et al. Nonlinear terahertz metamaterial perfect absorbers using GaAs [Invited]. Photonics Res 2016;4:A16–21.

[314] Jiang JL, Zhang X, Zhang W, et al. Polarized low-coherence interferometer based on a matrix CCD and birefringence crystal with a two-dimensional angle. Opt Express 2017;25:16867–78.

[315] Zhao HL, Ren GJ, Liu F, Xin HP, Bai YB, Yao JQ. Tunable terahertz source via liquid crystal grating coated with electron beam excited graphene: a theoretical analysis. Opt Commun 2017;390:137–9.

[316] Peres NMR, Bludov YV, Ferreira A, Vasilevskiy MI. Exact solution for square-wave grating covered with graphene: surface plasmon-polaritons in the terahertz range. J Phys-Condens Mat 2013;25:125303.

[317] Gu XF, Lin IT, Liu JM. Extremely confined terahertz surface plasmon-polaritons in graphene-metal structures. Appl Phys Lett 2013;103:071103.

[318] Zhao H, Guo Q, Xia F, Wang H. Two-dimensional materials for nanophotonics application. Nanophotonics 2015;4:128–42.

[319] Okamoto N. Reciprocity of electromagnetic waves scattered by anisotropic composite obstacles. J Appl Phys 1971;42:5465.

[320] Lee S, Park QH. Dynamic coupling of plasmonic resonators. Sci Rep 2016;6:21989.

[321] Bahk YM, Park HR, Ahn KJ, et al. Anomalous band formation in arrays of terahertz nanoresonators. Phys Rev Lett 2011;106:013902.

[322] Aydin K, Cakmak AO, Sahin L, et al. Split-ring-resonator-coupled enhanced transmission through a single subwavelength aperture. Phys Rev Lett 2009;102:013904.

[323] Li WD, Hu J, Chou SY. Extraordinary light transmission through opaque thin metal film with subwavelength holes blocked by metal disks. Opt Express 2011;19:21098–108.

[324] Cakmak AO, Aydin K, Colak E, et al. Enhanced transmission through a subwavelength aperture using metamaterials. Appl Phys Lett 2009;95:052103.

[325] Valdivia-Valero FJ, Nieto-Vesperinas M. Enhanced transmission through subwavelength apertures by excitation of particle localized plasmons and nanojets. Opt Express 2011;19:11545–57.

[326] Chen L, Wei YM, Zang XF, Zhu YM, Zhuang SL. Excitation of dark multipolar plasmonic resonances at terahertz frequencies. Sci Rep 2016;6:22027.

[327] Gao H, Cao Q, Zhu MN, Teng D, Shen SY. Nanofocusing of terahertz wave in a tapered hyperbolic metal waveguide. Opt Express 2014;22:32071–81.

[328] Lin RR, Xu YB, Liu HY, Lan S, Gopal AV. Strong localization of terahertz wave and significant enhancement in electric field achieved in U-shaped resonators with a large aspect ratio. Appl Phys Lett 2013;103:123505.

[329] Kim N. In S, Lee D, et al. Colossal terahertz field enhancement using split-ring resonators with a sub-10 nm gap. ACS Photonics 2018;5:278–83.